

[Click here to view linked References](#)

1 **The ultimate fate of a synmagmatic shear zone. Interplay**
2 **between rupturing and ductile flow in a cooling granite pluton.**

3 I Zibra, JC White, L Menegon, G Dering and K Gessner

4

5 Corresponding author: Ivan Zibra (ivan.zibra@dmirs.wa.gov.au)

6 Geological Survey of Western Australia

7 Department of Mines and Petroleum

8 100 Plain Street East Perth WA 6004

9 Tel: +61 8 9222 3082

10 Keywords:

11 Rupture; cataclasite; mylonite; tourmaline; transpression; strain partitioning

12 **Abstract**

13 The Neoproterozoic Cundimurra Pluton (Yilgarn Craton, Western Australia) was
14 emplaced incrementally along the transpressional Cundimurra Shear Zone.
15 During syndeformational cooling, discrete networks of cataclasites and
16 ultramytonites developed in the narrowest segment of the shear zone, showing
17 the same kinematics as the earlier synmagmatic structures. Lithological
18 boundaries between aplite/pegmatite veins and host granitic gneiss show more
19 intense pre-cataclasite fabrics than homogeneous material, and these boundaries
20 later became the preferred sites of shear rupture and cataclasite nucleation.

21 Transient ductile instabilities established along lithological boundaries culminated
22 in shear rupture at relatively high temperature (~500–600°C). Here, tensile
23 fractures at high angles from the fault plane formed asymmetrically on one side of
24 the fault, indicating development during seismic rupture, establishing the oldest
25 documented earthquake on Earth.

26 Tourmaline veins were emplaced during brittle shearing, but fluid pressure
27 probably played a minor role in brittle failure, as cataclasites are in places
28 tourmaline-free. Subsequent ductile deformation localized in the rheologically
29 weak tourmaline-rich aggregates, forming ultramytonites that deformed by grain-
30 size sensitive creep. The shape and width of the pluton/shear zone and the
31 regime of strain partitioning, induced by melt-present deformation and established
32 during pluton emplacement, played a key role in controlling the local distribution of
33 brittle and then ductile subsolidus structures.

34 **1 Introduction**

35

36 The mid- to upper continental crust, particularly during the early history of Earth, is
37 dominated by intermediate-to-felsic intrusive rocks (Christensen and Mooney,
38 1995), thus the deformation behaviour of such bodies is critical to understanding
39 of tectonic processes within continental lithosphere. Subsidiary strain localization
40 in granitic rocks can be summarised in terms of two different models. In one
41 model, strain hardening (Hobbs et al., 1990) or strain— and thermal—softening
42 (White et al., 1980; Mancktelow, 2002; Thielmann and Kaus, 2012; Jaquet and

43 Schmalholz, 2017) controls the nucleation of shear zones. Deformation is thereby
44 localised in an otherwise grossly isotropic medium lacking pervasive anisotropies
45 such as flow layering, foliations or fractures. In the second model, inherited and
46 precursor structures play a key role for localizing the development of ductile shear
47 zones (Christiansen and Pollard, 1997; Guermani and Pennacchioni, 1998;
48 Mancktelow and Pennacchioni, 2005; Pennacchioni and Mancktelow, 2007;
49 Menegon and Pennacchioni, 2010; Goncalves et al., 2016). In the past decade,
50 detailed field studies have demonstrated that anisotropies, such as cooling joints
51 and lithological boundaries, play a key role in controlling the development of
52 subsolidus shear zones in the mid-crust (Pennacchioni and Zucchi, 2013, and
53 references therein). However, most of these studies focussed on the development
54 of subsolidus outcrop- to grain-scale structures, so that the role of larger (i.e. km-
55 scale) structures developed during pluton emplacement, and the role of a pluton
56 itself in influencing the local strain distribution, is less well understood (Blanquat et
57 al., 2011). If fault initiation and propagation styles are scale-variant (Crider, 2015),
58 determining causes for strain localization at the regional scale, remains central to
59 achieving understanding about deformation in the intermediate to felsic igneous
60 rocks of the continental crust.

61 This contribution documents subsolidus deformation in the Neoproterozoic
62 Cundimurra Pluton, from the Yilgarn Craton of Western Australia. This pluton was
63 emplaced incrementally over a period of c. 20 Myr, along an active, triclinic
64 transpressional shear zone (the Cundimurra Shear Zone, CMSZ; (Zibra et al.,
65 2014b). The structures related to subsolidus overprinting exhibit the same
66 kinematics as the synmagmatic CMSZ and provide an exceptional opportunity to
67 examine the transiently discontinuous response within a ductile shear zone
68 undergoing syndeformational cooling. We show that the post-magmatic stages of
69 shear zone activity were characterized by the development of discrete fault
70 networks comprising cataclasites and ultramytonites. Both ductile and brittle
71 subsolidus structures are postdated by a c. 2620 Ma pluton, and are therefore of
72 Neoproterozoic age. We document brittle structures within regional-scale fault
73 networks containing evidence of a rupture episode at seismic velocities, with
74 subsequent aseismic displacement along cataclasites and ultramytonites.
75 Consequently, to the best of our knowledge, brittle faults within the CMSZ

76 preserve paleoseismic record of the oldest earthquakes yet documented on Earth.
77 Our data reveal that brittle behaviour was transient, with a return to ductile
78 deformation in the last stage. We propose that the regional-scale architecture of
79 the shear zone and the melt-induced strain partitioning of the bulk triclinic flow,
80 both of which were established during pluton emplacement, played a major role in
81 controlling the subsolidus evolution of the cooling pluton.

82 **2 Geological setting**

83 The Archean Yilgarn Craton of Western Australia consists of c. 3050–2600 Ma
84 granites and granitic gneisses associated with c. 3080–2650 Ma greenstone belts
85 (i.e. metamorphosed volcano-sedimentary sequences and gabbroic sills). Lu–Hf
86 and Sm–Nd isotopic data indicate that the craton recorded older crust-forming
87 events, dating back to c. 4200 Ma (Wyche et al., 2012). The craton has been
88 subdivided into several terranes on the basis of stratigraphic, structural,
89 geochemical and geochronological data (Cassidy et al., 2006; Fig. 1a). In the c.
90 2730–2620 Ma time span, a major episode of magmatism and crustal recycling
91 occurred during the Neoproterozoic Yilgarn Orogeny (Zibra et al., 2017a), and
92 resulted in the assembly of several terranes to form the Yilgarn Craton (Myers,
93 1995). Seismic profiles show that boundaries between different terrains are
94 represented by crustal-scale, east-dipping listric shear zones (Wilde et al., 1996;
95 Goleby et al., 2004; Wyche et al., 2013) that are sub-parallel to the internal
96 structural grain of each individual terrane.

97 In the western portion of the craton (Youanmi Terrane, Fig. 1a), such networks of
98 east-dipping crustal-scale shear zones accompanied the emplacement of large
99 batholiths, controlling the delivery of Tonalite–Trondhjemite–Granodiorite (TTG)
100 melt from its lower crustal source towards sink regions in the upper crust (Zibra et
101 al., 2014a, 2017a, 2017b). In the centre of the Youanmi Terrane, the dextral
102 transpressional Cundimurra Shear Zone (CMSZ, Fig. 1b) was active for >20 Myr,
103 during the incremental emplacement of the Cundimurra Pluton (Zibra et al.,
104 2014b). Displacement along the CMSZ continued after pluton assembly, during
105 the syndeformational cooling of the granite-greenstone system.

106 The main gneissic foliation in the CMSZ developed under lower amphibolite facies
107 conditions in both granites (S_{MT} ; moderate temperature foliation) and greenstones
108 (S_G ; figs 5–7 in Zibra et al., 2014b). Higher temperature (magmatic to solid-state)
109 fabrics are locally preserved, mainly in the central segment of the CMSZ. The
110 regional strain was strongly partitioned along the CMSZ, such that greenstone-
111 derived tectonites accommodated the bulk of horizontal shortening and dip-
112 parallel components of regional displacement, while granitic gneiss
113 accommodated the strike-parallel component (Fig. 1c). The strike-parallel-
114 dominated portion of the shear zone is ~17 km wide in the central and southern
115 portions of the pluton, narrowing to ~2.5 km in the northeast-trending,
116 northernmost part of the pluton (Fig.1b). The CMSZ extends for ~160 km north of
117 the study area, towards the northern margin of the craton (Fig.1a), where it is
118 truncated by Proterozoic structures. In its northern segment, outside of the study
119 area, the CMSZ is entirely developed within greenstone sequences, where it splits
120 into several synthetic branches, exploiting infra-greenstone lithological
121 boundaries. The CMSZ, as with all the structures in the area, is post-dated by the
122 c. 2620 Ma Garden Rock Monzogranite (“GR”, Fig.1b; Zibra et al., 2014b), which
123 shows concentric (i.e. pluton-parallel) magmatic foliation (inset d, Fig. 2),
124 discordant to the CMSZ.

125 **3 The Lake Austin Shear Zone: geometry and kinematics**

126 The Lake Austin Shear Zone (LASZ) is a composite strike-slip structure exposed
127 within the northern portion of the Cundimurra Pluton (Figs. 1 and 2). This structure
128 postdates S_{MT} , extends ~33 km along strike and is developed entirely within the
129 granitic gneiss. The LASZ postdates the c. 2660 Ma youngest leucogranite
130 component of the pluton (Zibra et al., 2014b) and shows no evidence of melt-
131 present deformation, being developed solely under subsolidus conditions.

132 Based on distinctive meso- and microstructures, the LASZ can be subdivided into
133 three domains, which are, from north to south, the Pinnacles fault, the Golconda
134 mylonite and the Moyagee fault (Fig. 2). The Moyagee and Pinnacles faults are
135 characterized by networks of discrete cataclasite and ultramylonite zones, and are
136 linked and postdated by the ~ 3 km-wide Golconda mylonite, which include

137 granitic gneiss whose fabric exhibits geometry and kinematics identical to S_{MT}
138 (Fig. 2).

139 **3.1 The Moyagee fault**

140

141 The Moyagee fault (Figs. 2 and 3) contains a network of cataclasites and
142 ultramytonites postdating S_{MT} . The network is sub-parallel to the western pluton
143 boundary. It is exposed for ~7.5 km along strike, with a maximum width of ~1.5
144 km, near its central portion. Scaling and topology of the fault array were
145 documented by integrating field observations with millimetre-resolution digital
146 orthoimagery, acquired by drone photogrammetry over an outcrop area of 900 m²,
147 in the best exposed, central portion of the Moyagee fault (Figs. 4a–c; see also
148 supplementary file A). Mapping shows that the metre-scale geometry of the fault
149 array is similar to that mapped at regional scale (compare Figs. 4a and b): main
150 fault segments are up to ~1–3.3 km-long, displaying an overall en-echelon
151 arrangement. They are oriented ~10° clockwise with respect to the shear zone
152 boundary, and are joined by shorter segments oriented ~15° counterclockwise
153 from them (i.e. R- and P-type orientations, respectively, Figs. 3a, b and e). At any
154 given scale, R-type shears consistently intersect S_{MT} at angles of 10°–25°
155 clockwise. However, orientation data overlap when plotted for the entire area
156 (compare Figs. 2a with 3c and 3d), masking the consistent angular relationship
157 between S_{MT} and fault surfaces that is found at each occurrence of the geometry.

158 **3.1.1 Brittle shear zones and veins**

159

160 Fault segments comprise 1–10 cm-thick cataclasites showing dense networks of
161 mm- to cm-thick dark tourmaline veins, containing a large proportion of gneiss
162 clasts (i.e. up to 50%), which are typically millimetres to centimetres in size.
163 Lateral veins branching off the main shear surfaces typically have millimetric to
164 submillimetric thickness (Figs. 5a and b). Main fault segments commonly occur in
165 paired shear systems (Figs. 4a–c, 5a–f) that are typically 0.5–1m apart, and are
166 oriented at low-angles to S_{MT} in the host gneiss (Fig. 3). Paired brittle faults
167 typically have main Y-shears joined by R-shears and subordinate P-shears, and
168 flanked by evenly spaced, high-angle T-fractures (Figs. 5a–c). At least some of

169 the smaller-scale shear surfaces likely represent former high-angle T-fractures,
170 attenuated during the subsequent ductile overprint that commonly focussed along
171 the lithological contacts (Fig. 5a). Tourmaline-rich veins typically occur in dilatant
172 sites and/or along principal slip surfaces (Fig. 5a). The volume of tourmaline veins
173 associated with cataclasites increases in domains with more intense brecciation
174 (compare Fig. 5b with Fig. 5f, which is likely representative of an incipient stage of
175 fracturing). Notably, cataclasites and ultramytonites are tourmaline-free in places
176 (Figs. 3a and 5g), and spatially associated with aplite and pegmatite veins. In the
177 few cataclasites that completely escaped the subsequent ductile overprint (Figs.
178 5b–d), both foliation and lineation (S_{CAT} and L_{CAT} , respectively) are defined by the
179 preferred orientation of granitic clasts in response to cataclastic flow. On
180 horizontal exposures, foliated domains show R-, R'-, P-shears and T-fractures,
181 shear bands and deflection of pre-existing foliation consistently indicate dextral
182 shear sense (Figs. 5a–f). Some shears in R'-orientation (Fig. 5d) may have
183 originated as tensile cracks that were subsequently reactivated as smaller-scale
184 shears during post-rupture cataclastic flow.

185 Fault segments terminate in zones of complex fracturing a few metres wide,
186 associated with horsetail splay systems (Figs. 5b–d), whose asymmetry with
187 respect to the main fault surfaces agrees with the observed dextral displacement.
188 Some fault segments include thicker veins (1–5 cm-thick, Fig. 5h), contain rare
189 gneiss clasts (0.1–1cm in size) and have thicker lateral veins (up to 1 cm-thick),
190 resembling injection veins of pseudotachylytes (Sibson, 1975; Swanson, 1988;
191 Rowe et al., 2012; and references therein). Of special note are sharp fault
192 contacts with tourmaline-filled periodic tensile fractures emanating from one side
193 only (Figs. 5b and c).

194

195 **3.1.2 Mylonites and ultramytonites**

196

197 Most cataclasites are partially to completely overprinted by 1–50 cm-wide
198 mylonites to ultramytonites. These ductile high-strain zones comprise SL
199 tectonites with sub-vertical foliation (S_U , ultramytonite foliation) and prominent

200 horizontal stretching lineation (L_U), sub-parallel to S_{MT} and L_{MT} in the host gneiss,
201 respectively (compare Figs. 2a and 3c). Mylonites are commonly paired with
202 cataclasites in an arrangement where one side of a pre-existing cataclasite band
203 preserves the dominantly brittle structures, whereas the other side exhibits a
204 mylonitic foliation (Fig. 6). The high-strain ductile shear zones are very localized
205 and the transition from cataclasite to ultramylonite is commonly sharp (Fig. 6).
206 Elongate gneiss clasts with aspect ratio > 100:1 are common along the median
207 zone of ultramylonites, defining a prominent compositional layering. On horizontal
208 surfaces, sigmoidal clasts, S-C fabric and C' shear bands invariably indicate
209 dextral shear sense (Figs. 5g, 6a and b). Veins at high-angle from the main fault
210 surfaces are moderately to steeply north-dipping (S_{OBL} , foliation bearing an
211 oblique stretching lineation, Fig.3d) and were commonly reactivated as reverse to
212 oblique-slip ultramylonites. Stretching lineation associated with these shear zones
213 (L_{OBL}) is at low angle from L_U (compare Figs. 3c and d).

214 **3.1.3 Nucleation of shear fractures: the role of** 215 **lithological contacts**

216
217 External to the Moyagee fault, granitic gneiss typically contains a compositional
218 layering formed of pegmatite and aplite veins oriented sub-parallel to S_{MT} (Fig.
219 7a). The common spatial association of cataclasites and aplites/pegmatites veins
220 within the Moyagee fault (Figs. 5a, h and 7b–d) suggests that such lithological
221 contacts were the preferred sites for cataclasite nucleation. The close spatial
222 relationship between aplite/pegmatite veins and brittle structures is preserved
223 even in the more common case of ductily sheared cataclasites (Fig. 7c), which
224 locally occur along both sides of an aplite/pegmatite vein (Fig. 7d). Along the
225 eastern margin of the Moyagee fault, pegmatite veins subparallel to S_{MT} show
226 pinch-and-swell and boudinage structures, along en-echelon array of dextral C'
227 shear bands (Fig. 7e and 7f). Here, C' shear bands are equally spaced (~7 cm
228 apart), ~1–5 mm-thick and ~50 cm in length, centred on the sheared felsic vein.
229 Each single shear band terminates ~20 cm away from the sheared pegmatite, by
230 progressively rotating into parallelism with the gneissic foliation or by developing
231 cm-long splays (Fig. 7f).

232 Some mylonitized cataclasites are not associated with tourmaline veins (Figs. 3a
233 and 5g), but are localized within 10–20 cm thick felsic veins (Fig. 7g). These
234 localized shear zones that can be followed for ~2 km along strike (stars in Fig. 3),
235 display dextral offsets of a few metres (Fig. 7g) and may show knife-sharp
236 boundaries against the host granitic gneiss (Fig. 7h). Importantly, such mylonitic
237 veins, with or without their brittle precursor, are not visible in the other domains of
238 the Cundimurra Shear Zone.

239 **3.2 The Pinnacles fault**

240

241 The Pinnacles fault is exposed at the northern tip of the Cundimurra Pluton (Fig.
242 2). At this locality, a network of granitic dykes is intruded into interlayered
243 ultramafic schist and amphibolite of the greenstone belt adjacent to the
244 Cundimurra Pluton (Fig. 8a). S_{MT} in the gneiss is truncated at a small angle by
245 tourmaline-bearing cataclasites, similar to those exposed along the Moyagee
246 fault. The gneiss-greenstone contact is marked by a ~1–3 m-thick quartz vein that
247 pre-dates tourmaline-bearing cataclasites. The complete sequence across the
248 contact is mylonitized, and a ~1 m-thick, tourmaline-bearing ultramylonitic
249 cataclasite occurs along the western (pluton) side of the quartz vein (Fig. 8a).
250 Within a ~15 m zone eastward from the quartz vein, mylonitic granite dykes were
251 boudinaged within the less competent ultramafic schists and likewise show
252 intense cataclasis/brecciation, associated with the introduction of tourmaline. This
253 rupture zone contains angular fragments of mylonitic dykes and the mylonitic
254 quartz vein (Figs. 8b–d). Millimetre-thick cataclasites, associated with
255 emplacement of thin tourmaline-rich veins, are also found in other boudinaged
256 dykes farther away from the granite-greenstone boundary (stars in Fig. 8a). On
257 the greenstone side of the deformed intrusive contact, no tourmaline-bearing
258 cataclasites were observed in either non-boudinaged granitic dykes or in host
259 mafic to ultramafic gneiss and schist. Tourmaline veins locally show incipient
260 domino-type boudinage (Fig. 8d; Goscombe and Passchier, 2003), suggesting
261 that minor deformation occurred after vein emplacement.

262

263 **3.3 The Golconda mylonite**

264

265 North of the Moyagee fault, the Golconda mylonite (Fig. 2) contains granitic
266 gneiss whose fabric exhibits geometry and kinematics identical to S_{MT} (compare
267 insets a and b, Fig. 2). However, the main ductile fabric in the Golconda mylonite
268 reflects accumulation of much larger amounts of strain than S_{MT} , evidenced by the
269 prominent and pervasively developed C fabric (Fig. 9a). Moreover, field
270 relationships indicate that the Golconda mylonite overprints cataclasites belonging
271 to both the Moyagee fault and the Pinnacles fault (Fig. 2 and 3), and therefore
272 postdates S_{MT} . This latter ductile deformation produced marked attenuation of
273 both the host gneiss fabric and the cataclasite/ultramylonite zones of the Moyagee
274 fault. Primary cataclasite structures are generally not preserved, but deformed
275 versions are detectable as tourmaline-bearing ultramylonites. The various
276 orientations of (Moyagee-related) Riedel fractures are rotated into parallelism with
277 the mylonitic fabric, and mylonitic folds with subhorizontal axes and subvertical
278 axial planes are common (Fig. 9b). Layered portions of ultramylonites locally
279 record domino-type boudinage (Goscombe and Passchier, 2003) whose geometry
280 is consistent with the generalized dextral shear sense observed in host, high-
281 strain granitic gneiss (Fig. 9c).

282 The ductile fabric in the Golconda mylonite is in turn postdated by discrete, dextral
283 strike-slip faults developed at a low angle to the prominent C fabric (Fig. 9d). Each
284 of the main fault segments extend a few metres along strike in an en echelon
285 arrangement and are linked by bridging (transfer) zones formed by closely spaced
286 fracture surfaces (Fig. 9e). The major fault surfaces are oriented $\sim 20^\circ$ clockwise
287 with respect to the primary C shear surfaces of the ductile fabric, i.e. an
288 orientation kinematically analogous with R-type synthetic shears in brittle shear
289 zones, with the ductile C orientation acting as Y-orientation at this scale. These
290 faults offset the main C fabric and are interpreted to have nucleated along C
291 surfaces, during the latter stages of slip. In Fig. 9d, right-stepping overlapping
292 regions developed extensional oversteps with pinnate fractures (Figs. 9e and f).
293 Observed displacement is about 1 m. Fault terminations show progressive
294 rotation of fault surface towards parallelism with the main C fabric in host gneiss,
295 with offset at fault tips accommodated by foliation-parallel slip. These faults

296 represent the youngest structures observed along the whole Lake Austin Shear
297 Zone.

298 **4 Microstructures**

299 We use representative microstructures from three samples to support mesoscopic
300 field observations. Although the study area clearly shows complex and protracted
301 evolution, we selected samples that provide an adequate first-order assessment
302 of the three main generations of fabrics across the northern portion of the CMSZ.
303 Sample 219356, from a boudinaged pegmatite within granitic gneiss (Figs. 7e and
304 f), is representative of the gneissic fabric predating the cataclasites. Sample
305 212762 contains a ~3 mm-thick cataclasite vein (developed at a high angle to S_{MT}
306 in host granitic gneiss) that does not show any evidence of ductile overprint.
307 Sample 212727 (section 4.3) represents a more evolved case containing a paired
308 cataclasite-ultramylonite.

309 SEM (Scanning Electron Microscopy), EDS (energy dispersive spectroscopy) and
310 EBSD (Electron Backscatter Diffraction, Prior et al., 1999) analysis of the
311 ultramylonite was performed on polished XZ thin sections using a Jeol LV6610
312 SEM at the Electron Microscopy Centre, Plymouth University. Thin sections were
313 chemically polished and carbon coated before acquisition of EBSD patterns.
314 EBSD patterns were acquired with the following working conditions: 15 kV
315 voltage, 70° sample tilt, working distance of 20 mm, and step size of 1.5 μm and
316 0.4 μm for polycrystalline quartz ribbons and ultrafine-grained tourmaline,
317 respectively. Quartz crystallographic preferred orientation (CPO) of sample
318 198170, showing similar microstructures as sample 212727, was obtained using
319 an automated fabric analyser microscope (G50-white; Peterneil et al., 2010). For
320 each pixel within the field of view, the G50 determines a unique orientation with a
321 resolution of 43 $\mu\text{m}/\text{pixel}$. Afterwards, for each single quartz grain a mean c-axis
322 orientation was selected with the freeware INVESTIGATOR software (Peterneil et
323 al., 2009).

324

325 **4.1 Pre-cataclasite microstructures in granite gneiss**

326

327 The salient microstructural features of S_{MT} are detailed in Zibra et al. (2014b), and
328 are summarized here. Both plagioclase and K-feldspar show grain size reduction
329 and overall evidence of deformation by low-temperature plasticity (Simpson,
330 1985), locally including microfractures and incipient core-and-mantle
331 microstructure associated with albite + K-feldspar new grains (~2–20 μm in size).
332 Recrystallized quartz grains are mostly in the 100–500 μm grain size range.

333 Sample 219356 is representative of the pinch-and-swell and boudinage structure
334 developed along the boundaries between pegmatite veins and host granitic
335 gneiss (Figs. 7e, 10a and B1). This sample recorded a domainal, bimodal
336 microstructure. The granitic gneiss show incipient grain-size reduction, with mm-
337 long lenses of recrystallized quartz aggregates wrapping around feldspar
338 porphyroclasts. Lensoid quartz ribbons generally do not form along-strike
339 continuous layers, and include aggregates of amoeboid to polygonal grains with
340 grain size in ~100–500 μm interval, but with ~60–70% of grains clustering around
341 100–200 μm (Fig. 10b). Plagioclase and K-feldspar show comparable deformation
342 features, with $\geq 80\%$ of porphyroclasts showing evidence of incipient to
343 widespread microfracturing (Figs. 10a and b), with both domino-type and shear
344 band type fragmented porphyroclasts. In K-feldspar porphyroclasts, antithetic
345 microfractures are mostly sub-parallel and equally spaced, suggesting that their
346 development was crystallographically-controlled (Fig. 10b). Trails of feldspar
347 aggregates (equant albite–oligoclase and orthoclase grains, 10–15 μm in size)
348 coat microfractures and wrap around angular feldspar fragments (Fig. 10c). In
349 striking contrast with such coarse-grained, protomylonitic foliation that typify the
350 granitic gneiss, shear bands in C' orientation developed along the pegmatite
351 margins (Figs. 7f and 10a) consist of mm-thick ultramylonite that sharply truncate
352 S_{MT} (Fig. 10d). Ultramylonite contains aligned flakes of recrystallized biotite and
353 muscovite, within an ultrafine matrix of equant feldspar (10–20 μm in size) and
354 lensoid quartz ribbons (grain size: 50–100 μm).

355

356 **4.2 Cataclasites**

357

358 The cataclasite (sample 212762, [Figs. 10e–h](#) and [Supplementary Materials B2](#)) is
359 from a lateral vein branching off at high-angle from a main fault surface.
360 Microstructural features of the pre-cataclasite gneissic foliation (S_{MT}) in this
361 sample are comparable to those described in the previous section. The
362 background fabric is truncated by a ~3 mm-thick, dark cataclasite vein, developed
363 at ~45° from S_{MT} ([Fig. 10e](#)). The vein shows irregular margins and locally contains
364 large, anhedral tourmaline₁ grains (up to 2–3 mm in size), set within a fine-grained
365 matrix mainly composed of tourmaline₂, muscovite, biotite, opaque phases and
366 angular to rounded clasts of the host gneiss ([Fig. 10f](#)). Tourmaline₂ occur as ~5–
367 100 µm euhedral and randomly-oriented grains that completely
368 pseudomorphosed tourmaline₁, largely overgrowing other phases in the vein
369 matrix. Lateral veins departing from the main cataclasite are ~10–100 µm thick
370 and are associated with intensely developed fractures in both quartz and
371 feldspars in the host gneiss. The portion of granitic gneiss flanking the cataclasite
372 contains ultramylonite layers composed of completely recrystallized feldspar (10–
373 20 µm in size) and lensoid quartz ribbons containing polygonal, strain free grains
374 ([Figs. 10f, g](#) and [B2](#)). Angular clasts of ultramylonite occur within the cataclasite,
375 and thin, tourmaline-bearing cataclasite veins, branching off the main surface,
376 postdate ultramylonite ([Figs. 10g](#) and [h](#)).

377

378 **4.3. Ultramylonites**

379 The ultramylonite sample 212727 ([Figs. 6b](#) and [11a](#)) is representative of paired,
380 tourmaline-bearing cataclasites-ultramylonites. The eastern side of the shear zone
381 preserves cataclastic microstructures, and includes a dense network of veins both
382 sub-parallel and at high angle to the main vein, containing angular fragments of
383 host gneiss, ranging in size from a few µm to several mm. The mineral
384 assemblage of these veins is comparable to that of the cataclasite (sample
385 212762). Even veins that are at a high angle (30–50°) to the main vein are locally
386 overprinted by mylonitic deformation and show elongated polycrystalline quartz
387 ribbons wrapped by the tourmaline-rich matrix ([Fig. 11b](#)). Feldspar and quartz in
388 the damage zone flanking the veins are dissected along a network of fractures
389 ranging in width from a few microns to ~100 µm.

390 The opposing western side of the main tourmaline-bearing vein is overprinted by a
391 cm-thick ductile shear zone. The margin of the vein is moderately deformed and
392 most gneiss clasts within the vein have acquired a sigmoidal shape or have long
393 axes inclined to the vein margin, in agreement with the dextral shear sense
394 observable at outcrop scale. The transition from mylonite, near the margin of the
395 vein, to ultramylonite occurs over ~2 mm. The mylonite layer contains σ -shaped
396 feldspar porphyroclasts, up to ~400 μm in size, set in a fine-grained matrix
397 composed of recrystallized feldspar, quartz, muscovite and tourmaline₂. Lensoid
398 quartz ribbons are several millimetres long and typically one-grain thick, and
399 quartz grains are ~40–200 μm in size. Feldspar porphyroclasts show patchy
400 undulose extinction and microfractures and are wrapped by aggregates of albite–
401 oligoclase and orthoclase equant grains, ~10–20 μm in size. Transposed T₁ veins
402 contain boudinaged tourmaline₁ porphyroclasts and ultrafine tourmaline₂
403 aggregates (grain size: \ll 1–10 μm) aligned sub-parallel to S_U. Here, most
404 feldspar porphyroclasts show synthetic microfractures (i.e. shear band type clasts,
405 Fig. 11c).

406 In the centre of the ductile shear zone, the transition to the ~1 cm-thick
407 ultramylonite layer occurs through gradual disappearance of feldspar
408 porphyroclasts and through an increase in transposed tourmaline veins (Figs. 11d
409 and e). The one-grain thick quartz ribbons at the mylonite-ultramylonite transition
410 as well as within the ultramylonites contain nearly equant quartz grains, 30–50 μm
411 in size, and show pinch-and-swell and boudinage microstructures, with boudin
412 neck filled by K-feldspar (Figs. 11d–f). The ultramylonite matrix is dominated by
413 ultrafine-grained tourmaline₂ (grain size: <1–20 μm , Fig. 11g) and contains also
414 equant quartz and feldspar grains with dispersed biotite and muscovite flakes of
415 comparable size. In places, euhedral tourmaline₂ crystals are concentrated in
416 microlayers, defining a compositional layering parallel to S_U (Figs. 11h and i).
417 Ultramylonites locally contain elongate quartz grains and opaque aggregates up
418 to 1 mm in size aligned parallel to incipient shear bands (Fig. 11i). A similar
419 microstructure is described in Menegon et al. (2015), in a monzonite ultramylonite
420 from Lofoten, northern Norway.

421 The c-axes of quartz grains in the monomineralic, polycrystalline, 20–100 μm
422 thick ribbons in the ultramylonite (e.g. **Figs. 11d and g**) define a crossed-girdle
423 fabric (Lister, 1977) with an opening angle of $\sim 70\text{--}75^\circ$ (**Fig. 12a**), suggesting
424 maximum deformation temperature of $\sim 600 \pm 50^\circ\text{C}$ (fig. 2 in Law, 2014). The a-
425 axes have a maximum at low angle to the stretching lineation, and the poles to the
426 prism- and rhomb planes have maxima subparallel to the foliation.

427 Tourmaline grains in the ultramylonite matrix are preferentially elongated at $\sim 30^\circ$
428 from the trace of the ultramylonite boundary, measured anticlockwise. This
429 defines a strong shape-preferred orientation (SPO) consistent with the dextral
430 shear sense the sample (**Fig. 12b**). Tourmaline grains are preferentially oriented
431 with their c-axis subparallel to the stretching lineation and with the poles to the
432 prism planes distributed on a girdle parallel to the YZ plane of finite strain ellipsoid
433 (**Fig. 12c**). Low-angle boundaries (misorientation: $2^\circ\text{--}10^\circ$) are scarce and
434 preferentially occur in relatively large grains (10–20 μm in length, **Fig. 12b**).

435 Microstructures from the Golconda mylonite are similar to those in the cataclasite-
436 derived ultramylonites.

437

438 **5 Discussion**

439 **5.1 The Moyagee and Pinnacles faults. Localization of brittle** 440 **rupture along ductile precursors**

441

442 **5.1.1 Localization of shear deformation at lithological boundaries**

443

444

445 The ~ 7 km-long Moyagee fault forms an en echelon array of overstepping, dextral
446 R-type shears ($\sim 1\text{--}3$ km-long) joined by shorter, synthetic P-orientation shears
447 (~ 0.5 km-long, **Fig. 3a and b**; Ahlgren, 2001 and references therein). This
448 geometry is repeated from map-scale down to the sub-metric scale (**Figs. 4a–d**.
449 **See also plates 1–4 in appendix A**). Observations from the margins of the fault
450 network indicate that lithological boundaries between felsic veins and host granitic
451 gneiss commonly exhibit more intense pre-cataclasite fabrics than within the
452 volume of adjacent lithologies (**Figs. 7e and f, 10a–d and B1**). In fact, we show

453 that, before the development of the Moyagee and Pinnacles faults, lithological
454 contacts recorded very heterogeneous strain. Shearing within the granitic gneiss
455 was accommodated by widespread recrystallization and dislocation creep in the
456 weaker quartz layers, while plagioclase and K-feldspar experienced widespread
457 fracturing in combination with fine-grained recrystallization (Figs. 10b and c).
458 Notably, microstructures show that quartz lenses did not coalesce to develop an
459 along-strike interconnected network of ribbons (Figs. 10b and Supplementary
460 Materials B1), suggesting that the rheology of the “strong” feldspar porphyroclasts
461 played a major role in controlling the bulk rheology of the granitic aggregate,
462 because a load-bearing framework of strong phases existed (Handy, 1990). In
463 contrast, lithological contacts between felsic veins and host gneiss were clearly
464 the sites of dramatic strain softening and were the loci for the development of
465 ultramylonites dominated by ultrafine feldspar (10–50 μm in size) and syntectonic
466 biotite and muscovite flakes (Fig. 10d and Supplementary Materials B1).
467 We propose that lithological boundaries between felsic veins and host granite
468 gneiss preferentially concentrated strain, similar to what is typically observed in
469 many other granitoids (e.g. (White, 1996, 2012; Pennacchioni and Mancktelow,
470 2007) and at biomechanical interfaces in other lithologies (White, 2003; Kelemen
471 and Hirth, 2007). This behaviour would have occurred by a combination of strain
472 hardening along the bi-material interface, and a consequent increase and
473 enhanced heterogeneity in the stress/strain rate distribution that in turn drove the
474 textural changes that resulted in weakening and strain localization.

475 5.1.2 Deformation overprinting

476
477 Along the Moyagee fault, abundant evidence that these same lithological
478 boundaries later became the preferred sites of cataclasite nucleation on discrete
479 rupture surfaces (Fig. 13a). Microstructures from non-mylonitized cataclasite (Fig.
480 10e–h and Supplementary Materials B2) show that pre-cataclasite ultramylonite
481 layers might have played a key role in controlling the nucleation of brittle
482 structures. Several studies indicate that ductile strain localization in granitic rocks
483 can be strongly controlled by pre-existing planar heterogeneities, lithological
484 boundaries and brittle precursor structures (Mancktelow and Pennacchioni, 2005;
485 Pennacchioni and Mancktelow, 2007; Pennacchioni and Zucchi, 2013). In

486 contrast, pre-existing ductile shear zones and lithological boundaries do not
487 necessarily control the nucleation of brittle faults in granitoids, and are often cut,
488 even at a very low angle, by subsequent fractures and faults (e.g., Pennacchioni
489 and Mancktelow, 2013). In contrast, the Moyagee fault represents a case where
490 cataclasites formed in an otherwise ductile regime, were spatially and temporally
491 coeval with ductile strain concentrations and were subsequently mylonitized. This
492 outcome suggests that a transient rheological behaviour, and not only the
493 geometry of precursor structures, played an important role in the generation of
494 cataclasites along the Moyagee fault (White, 1996, 2003, 2004, 2005, 2012;
495 Kelemen and Hirth, 2007; Stewart and Miranda, 2017).

496 The transition from dominantly ductile to brittle deformation may require the
497 development of ductile fractures (Weinberg and Regenauer-Lieb, 2010).
498 Coalescence of microvoids generated via intergranular fracturing, during
499 deformation of feldspar in the brittle–ductile transition, can lead to development of
500 rupture zones focussed in domains characterized by strong plastic deformation
501 (Shigematsu et al., 2004). The process of ductile fracturing may account for the
502 nucleation of the brittle structures described in this paper.

503 Brittle structures in granitic gneiss of the Pinnacles fault are similar to those
504 observed along the Moyagee fault. The greenstone portion of this fault segment
505 shows that tourmaline-bearing cataclasite only developed where the competent
506 granite dykes were boudinaged within the weak schistose matrix (Figs. 8a–c). As
507 for the Moyagee fault, syntectonic dilatancy generated during dyke boudinage
508 enabled emplacement of tourmaline-rich fluids.

509 **5.1.3 Occurrence of dynamic rupture**

510
511 Evidence for seismic rupture resides in the tensile fractures that form
512 asymmetrically on one side of a primary shear plane. Other studies have shown
513 that these periodic arrays are a product of dynamic rupture propagation (Di Toro
514 et al., 2005; Griffith et al., 2009; Rowe and Griffith, 2015 and references therein).
515 The preservation of these often-delicate structures highlights the high-degree of
516 preservation of the complete fault history. The infilling of these fractures by
517 tourmaline enhances their outward similarity with pseudotachylyte-filled fractures
518 (Fig. 5c), and is consistent with the simultaneous to near-simultaneous formation

519 of rupture and veins. However, we must note that, in the case described by Di
520 Toro et al. (2005), pseudotachylyte veins provided an independent evidence for
521 slip at seismic slip rates. On the other hand, recent studies show that
522 pseudotachylyte is no longer considered the only indicator of fossilized
523 earthquake ruptures (Rowe and Griffith, 2015). Consequently, the fault network
524 studied here contains paleoseismic record of the oldest earthquakes yet
525 documented on Earth. We infer that evidence for dynamic rupture is only rarely
526 preserved along the LASZ (Fig. 5c) since the indicative features are mostly
527 masked by both cataclasites and ultramylonites (Fig. 13).

528 Any positive feedback between strain hardening along lithological boundaries, a
529 consequent increase and enhanced heterogeneity in the stress distribution, in turn
530 driving the textural changes that resulted in weakening and strain localization,
531 may have produced greatly enhanced strain rate. This behaviour in turn may have
532 culminated in shear rupture at the relatively high temperature ($\sim 600 \pm 50^\circ\text{C}$) that
533 prevailed during the development of the main brittle-then ductile structures in the
534 study area. There need not be a direct path from ductile-to-brittle shear, and
535 cataclasites may have simply developed at mechanical anisotropies (C-surfaces)
536 associated with ductile strain concentration (Shigematsu et al., 2004). However,
537 direct transition through ductile rupture is not precluded. Notwithstanding the
538 evidence for initial seismic rupture, the transition to cataclasis and ductile shear
539 points to aseismic slip along the weak discontinuity, i.e. the initial rupture surface.

540 Although tourmaline veins typically demarcate the zones of localized deformation,
541 both discrete shear fractures and high-strain zones are not always associated with
542 such veins (Figs. 3, 5g, 7g and h). In the first instance, tourmaline introduction
543 appears to be associated with dilatancy during brittle failure (i.e. compare Figs. 5a
544 and b). Although fluid pressure would have played a role, we interpret the
545 fractures to be stress-driven, as opposed to fluid-pressure-driven (Cox and
546 Munroe, 2016), given the similarity of barren and tourmaline-bearing shear
547 fractures. This interpretation is consistent with the presence of systematic arrays
548 of synthetic R- and P-shears, which represent the typical geometric arrangement
549 of synthetic-driven Riedel shear zones, predicted by classical failure models (Figs.
550 2 and 3; Tchalenko and Ambraseys, 1970). Therefore, we conclude that
551 tourmaline-rich fluids were “passively” emplaced in dilational sites during brittle

552 shearing. Therefore, while the contribution of fluid pressure cannot be excluded
553 from triggering rupture, in this case we consider it unlikely to have played a
554 dominant role in the ductile-to-brittle transition.

555

556 **5.2 Evolution of the Lake Austin Shear Zone**

557

558 Field and microstructural evidence indicate that most ultramylonites exploited pre-
559 existing faults with cataclasites, which is best expressed in partial overprinting (i.e.
560 paired cataclasites-ultramylonites, Figs. 5g, 6a, b and 11a) and tourmaline-
561 bearing, layered ultramylonites (Figs. 7c, d, 9b and c). For complete ductile
562 overprints, evidence for the cataclasite precursors is preserved as tourmaline-
563 bearing, layered ultramylonites and attenuated, tourmaline-bearing T-fractures
564 (Figs. 6a and b, 7c, d, 9b and c). Brittle fault segments showing limited cataclasis
565 and small volumes of tourmaline-rich veins may represent brittle structures that
566 experienced insufficient deformation to become fully developed, while greater
567 accumulated brittle displacement was likely associated with the emplacement of
568 larger volumes of tourmaline (compare Figs. 5a and b). In both the Moyagee and
569 Pinnacles faults, cataclasite-derived ultramylonites show the same kinematics as
570 the solid-state deformation recorded within the Cundimurra Shear Zone (S_{MT} ,
571 compare Figs. 2a, 3c, 8a and 13). In these areas, deformation was extremely
572 heterogeneous, so that granitic gneiss flanking ultramylonites retain their pre-
573 cataclasite, homogeneous gneissic foliation (S_{MT} , e.g. Fig. 7h). Both faults with
574 their brittle-then-ductile heterogeneous shear are overprinted by ductile structures
575 along the Golconda mylonite, i.e. a 4 km-wide high-strain zone marked by
576 homogeneous fabric and prominent C-orientation shear bands (Fig. 9a).

577 We therefore propose the following multi-step evolution (Fig. 13) for the
578 subsolidus structural evolution of the CMSZ. After pluton crystallization,
579 subsolidus fabrics developed at high- and then moderate-temperature (S_{HT} and
580 S_{MT} , respectively, Zibra et al., 2014b), during progressive cooling. The switch from
581 S_{HT} to S_{MT} reflects a major rheological transition in feldspar, from steady-state
582 dislocation creep to low-temperature plasticity (based on a comparison of coarse

583 grains with interlobate boundaries and undulose extinction in Fig. 14c of Zibra et
584 al. (2014b) with the observation of finer, equant grains in mixed polyphase arrays
585 in Fig. 15b in Zibra et al. (2014b). Such a transition is anticipated to enhance
586 competency contrast between pegmatites/aplite veins and host gneiss, promoting
587 a transition, either directly or as preferred sites for stress heterogeneity, to seismic
588 rupture and cataclasis (Figs. 7e, f and 13a), which eventually led to the
589 development of km-scale brittle shear zone networks (i.e. Moyagee and Pinnacles
590 faults, Fig. 13b) in Riedel orientations (~parallel to C-surfaces) relative to the
591 regional shear zone boundary (Figs. 3a and b). Extensive fracturing of feldspar
592 promoting the formation of fine-grained C- and C' bands that subsequently
593 localized ultramylonitic deformation in granitoid mylonites was described by
594 Viegas et al. (2016). The substantive change in material properties triggered by
595 cataclasis and introduction of tourmaline, with no change in external conditions
596 (i.e. P and T), produced ultramylonites at the expenses of cataclasites (Figs. 6a
597 and b).

598 The tendency for reversion to ductile deformation reflects: (1) the combined
599 softening effect produced by faulting and grain-size reduction; plus (2) the overall
600 conditions in the Golconda mylonite region that supported bulk ductile shear
601 through the development of the penetrative S/C fabric. Several studies of
602 deformation at the frictional-viscous transition in the granitoid middle crust have
603 consistently concluded that the main rheological effect of brittle grain-size
604 reduction is to activate grain-size sensitive creep in the resulting fine-grained
605 material during viscous deformation (Fitz Gerald and Stünitz, 1993; Füsseis and
606 Handy, 2008; Viegas et al., 2016; Wehrens et al., 2016). Likewise, we interpret
607 the strong shape- and crystallographic preferred orientation of tourmaline in the
608 ultramylonites ([001] parallel to elongation of grains and to stretching lineation) as
609 the result of oriented grain growth coupled with grain rotation during diffusion
610 creep (Bons and den Brok, 2000; Getsinger and Hirth, 2014; Negrini et al., 2014).
611 This interpretation is supported by the lack of low-angle boundaries in the
612 tourmaline grains, with a very few exceptions (Fig. 12b), which indicates that the
613 grains are essentially strain free. Thus, the ultrafine-grained tourmaline-rich
614 mixture represented the rheological weak phase of the ultramylonite, whereas
615 monomineralic quartz ribbons deforming by dislocation creep were clearly

616 stronger because they underwent boudinage and pinch-and-swell (Figs. 11e–g).
617 This observation is in line with recent studies, which highlight that although quartz
618 deforming by dislocation creep is commonly assumed to represent the weak
619 phase controlling the rheology of the middle crust, fine-grained polyphase
620 mixtures typically found in ultramylonites are weaker than quartz and deform at
621 faster strain rates than monomineralic quartz domains (Kilian et al., 2011; Platt,
622 2015; Viegas et al., 2016).

623 The transition from localized (Moyagee and Pinnacles faults) towards diffuse
624 (Golconda mylonite) deformation (Fig. 13c) might simply have resulted from the
625 coalescence of ductile shear strain during progressive deformation. An
626 anastomosing network of narrow shear zones is anticipated to accommodate
627 limited amounts of finite displacement on each strand; volumetrically large
628 distributed strains would be attained through broadening of the deforming zone,
629 which eventually evolve into a zone of more distributed deformation (White, 1996;
630 Mancktelow, 2002; Pennacchioni and Mancktelow, 2007; Menegon and
631 Pennacchioni, 2010).

632 In summary, the simple generation of transient brittle discontinuities within a
633 continuously active ductile shear zone was concentrated in the region of the
634 Golconda mylonite and the resulting weakening induced by the grain-size
635 reduction could explain the ductile-brittle-ductile overprint relationships. The
636 structural evolution that we infer is consistent with continuous syndeformational
637 emplacement and cooling such that all fabrics of any given stage exhibit invariable
638 kinematics (Fig. 13d).

639

640 **5.3 Deformation framework and the role of emplacement-related** 641 **structures**

642

643 The dominant deformation mode during the syntectonic emplacement of the
644 Cundimurra pluton is one of viscous flow that occurred during both for the earliest
645 magmatic (Zibra et al., 2014b) and later dominant solid-state fabrics. The
646 distinctive fabric elements in order of formation are: magmatic flow foliations

647 (compositional layering including shear band structures); solid-state deformation
648 producing the background S_{MT} and oblique C-surfaces (shear bands); cataclasites
649 that disrupt S_{MT} ; mylonites and ultramylonites that form on pre-existing
650 cataclasites; and a high-strain analogue of S_{MT} (the Golconda mylonite) with
651 pervasive C-surface development that overprints S_{MT} and the localized
652 cataclasite/ultramylonite zones. Lastly, the latter high strain zone is itself subject
653 to faulting (Figs. 9d–f). This sequence is clearly an example of emplacement
654 concomitant with deformation, where deformation outlasted pluton crystallization.

655 A striking aspect of the LASZ is the monotonic nature of its kinematic evolution,
656 from magmatic flow stage through solid-state deformation and transient brittle
657 rupture (Fig. 13). The basic components of this history are an effectively constant
658 granitoid composition, syndeformational cooling and a fixed movement picture,
659 which includes dextral displacement. The nature and intensity of fabrics observed
660 are a function of finite strain intensity and mode of deformation. Ductile fabrics
661 exhibit S-C fabrics with the intensity and spacing of C-planes varying with finite
662 strain. The obliquity of the C-surface to the shear zone boundary, as defined by
663 regional lithological boundaries, is commonly used to denote it as the C'
664 orientation, though its formation in this orientation is simply the result of the bulk
665 triclinic kinematics (Lister and Snoke, 1984; Jiang and White, 1995). The primary
666 shear direction lies within the C-surfaces and parallel its intersection with the
667 sectional vorticity normal plane, consistent with the orientation of the stretching
668 lineations recorded throughout the area (e.g. Figs. 2 and 3).

669 Brittle behaviour was transient, being preceded and followed by the dominant
670 viscous deformation in all instances (e.g. Fig. 9a–c) but the last deformation stage
671 (Figs. 9d–f). Decreasing temperature, increasingly heterogeneous bulk fabric and
672 microstructural changes may have induced strain rate/stress changes, leading to
673 the transient brittle behaviour. Brittle rupture nucleated in this ductile volume as a
674 function of ductile flow (Weinberg and Regenauer-Lieb, 2010), rather than
675 propagating into the volume from out of a more brittle volume above that is often
676 found to be the case in other deforming rock volumes near the crustal brittle-
677 ductile transition. Thus, the observed structures are a continuum of behaviour that
678 reflects transient temporal and spatial partitioning of strain rate and strain.

679 Brittle behaviour within the CMSZ was transient, with transition from and reversion
680 to dominantly viscous deformation (e.g. Fig. 9a–c) in all but the last deformation
681 stage (Figs. 9d–f); that is, ductile flow was the precursor state for nucleation of
682 brittle rupture within the CMSZ (e.g. Weinberg and Regenauer-Lieb, 2010). That
683 the brittle faults formed within an ambient ductile regime is demonstrated by their
684 overprint by ductile deformation on a regional scale. The ductile-brittle-ductile
685 transition was a local, transient change in rheological response, rather than the
686 result of gross changes in crustal conditions. The variations in parameters such as
687 temperature (decreasing), bulk fabric (increasingly heterogeneous) and
688 microstructure (generally finer grained, more deformed) during shear zone
689 evolution necessarily influenced the rheological response through their control of
690 micromechanical processes. In turn, the feedback among such processes (e.g.
691 Kelemen and Hirth, 2007) may have induced strain rate/stress variations,
692 amplified in the absence of dampening conditions that would have produced
693 uniform, steady-state flow. The heterogeneity of micro- and macro-structures
694 argues against uniform behaviour, despite the long-term consistency of the
695 kinematic framework. Instead, the observed structures (foliated granitoids,
696 mylonites, shear fractures) form a continuum that reflects secular partitioning of
697 strain rate, and necessarily strain, as a result of intrinsic lithological
698 heterogeneities, such as aplite and pegmatite dykes, within the granitic body.

699 Two first-order features, established during pluton emplacement, played a major
700 role in controlling the subsolidus evolution of the cooling pluton. Firstly, the
701 Cundimurra Pluton/shear zone is a ~185 km-long, wedge-shaped body, varying in
702 width from a maximum of ~30 km in its southern portion, to a minimum of less
703 than 3 km near its northern domain (Figs. 1b and 2). Secondly, initial melt-induced
704 strain partitioning confined the strike-slip component of shearing within the pluton
705 (Fig. 1c; compare also orientation data for granitic gneiss and greenstones, Fig. 2,
706 insets a and c, respectively). Strain partitioning persisted during subsolidus
707 deformation, so that no visible strike-slip-related structures developed in the
708 greenstone component of the CMSZ, neither during pluton emplacement nor
709 retrograde shearing (Zibra et al., 2014b). These factors likely account for the
710 development of the Lake Austin Shear Zone in the narrowest segment of the
711 Cundimurra pluton/shear zone (Fig. 2). Bulk shear strain rate across a shear zone

712 is defined as the ratio between the particle velocity (v) and the shear zone width
713 (w). If boundary conditions maintained an approximately constant velocity, then a
714 decrease in width of the accommodation zone would have required a local
715 increase in strain rate in the LASZ portion of the CMSZ. Heterogeneous
716 partitioning of the strain rate, potentially with local fluctuations, may have in turn
717 have triggered the onset of brittle deformation at relatively high temperature.

718

719 **6 Conclusions**

720

721 This study examines the multistage evolution of the large-scale and long-lived
722 Cundimurra Shear Zone. During the syn-magmatic stages, transpressional
723 deformation was accommodated within a broad high-strain zone (>200 km in
724 length and 3–30 km in width), where the syntectonic Cundimurra pluton
725 partitioned the dextral slip component of shearing. With the cessation of
726 magmatism, syndeformational cooling of the shear zone induced dramatic strain
727 concentration in the narrowest portion of the pluton, where the superposed
728 generations of structures document the cyclical transition from dominantly ductile
729 to brittle behaviour. This study suggests that transient ductile instabilities
730 established along lithological boundaries culminated in seismic shear rupture at
731 relatively high temperature (~500°C). Our study therefore supports the view that
732 local heterogeneities (mainly pegmatites, aplite veins, and synkinematic
733 cataclasites formed in an overall ductile deformation regime) played an important
734 role in controlling nucleation and development of subsolidus high-strain zones.
735 Just as importantly, this work suggests that the regional (i.e. 10–10² km)
736 architecture established during pluton emplacement, in the form of shape and
737 width of the pluton/shear zone, and the regime of strain partitioning, induced by
738 melt-present deformation, played a key role in controlling the local distribution of
739 brittle and then ductile subsolidus structures.

740

741 **Acknowledgements**

742 We thank Virginia Toy and Federico Farina for very helpful and constructive
743 reviews that substantially improved the clarity of this contribution. We also thank
744 the Editor William M. Dunne for prompt handling of the manuscript and for the
745 additional, very careful and constructive review of the second version of this
746 paper. M. Prause and M. Jones helped in preparing the figures. P. Vota, T. Zama
747 and D. Twist provided invaluable support during fieldwork. This work benefited
748 from numerous field discussions with J.H. Kruhl, A. Ord, C. Passchier, M.
749 Peternell, S. Piazzolo and R. Weinberg. We thank them all. JCW was supported by
750 a NSERC Canada Discovery Grant. LM was supported by an FP7 Marie Curie
751 Career Integration Grant (grant agreement PCIG13-GA-2013-618289). The staff
752 at the Plymouth University Electron Microscopy Centre is thanked for support
753 during SEM analysis. The paper is published with the permission of the executive
754 director of the Geological Survey of Western Australia.

755 **References**

- 756 Ahlgren, S.G., 2001. The nucleation and evolution of Riedel shear zones as
757 deformation bands in porous sandstone. *Journal of Structural Geology* 23,
758 1203–1214. [https://doi.org/10.1016/S0191-8141\(00\)00183-8](https://doi.org/10.1016/S0191-8141(00)00183-8)
- 759 Blanquat, M. de Saint, Horsman, E., Habert, G., Morgan, S., Vanderhaeghe, O.,
760 Law, R., Tikoff, B., 2011. Multiscale magmatic cyclicity, duration of pluton
761 construction, and the paradoxical relationship between tectonism and
762 plutonism in continental arcs. *Tectonophysics* 500, 20–33.
763 <https://doi.org/10.1016/j.tecto.2009.12.009>
- 764 Bons, P.D., den Brok, B., 2000. Crystallographic preferred orientation
765 development by dissolution–precipitation creep. *Journal of Structural Geology*
766 22, 1713–1722. [https://doi.org/10.1016/S0191-8141\(00\)00075-4](https://doi.org/10.1016/S0191-8141(00)00075-4)
- 767 Cassidy, K., Champion, D., Krapez, B., Barley, M., 2006. A revised geological
768 framework for the Yilgarn Craton, Western Australia, Geological Survey of
769 Western Australia, Record 8(8).
- 770 Christensen, N.I., Mooney, W.D., 1995. Seismic velocity structure and
771 composition of the continental crust: A global view. *Journal of Geophysical*

772 Research: Solid Earth 100, 9761–9788. <https://doi.org/10.1029/95JB00259>

773 Christiansen, P.P., Pollard, D.D., 1997. Nucleation, growth and structural
774 development of mylonitic shear zones in granitic rock. *Journal of Structural*
775 *Geology* 19, 1159–1172. [https://doi.org/10.1016/S0191-8141\(97\)00025-4](https://doi.org/10.1016/S0191-8141(97)00025-4)

776 Cox, S.F., Munroe, S.M., 2016. Breccia formation by particle fluidization in fault
777 zones: Implications for transitory, rupture-controlled fluid flow regimes in
778 hydrothermal systems. *American Journal of Science* 316, 241–278.
779 <https://doi.org/10.2475/03.2016.02>

780 Crider, J.G., 2015. The initiation of brittle faults in crystalline rock., *Journal of*
781 *Structural Geology*. <https://doi.org/10.1016/j.jsg.2015.05.001>

782 Di Toro, G., Nielsen, S., Pennacchioni, G., 2005. Earthquake rupture dynamics
783 frozen in exhumed ancient faults. *Nature* 436, 1009–1012.
784 <https://doi.org/10.1038/nature03910>

785 Fitz Gerald, J.D., Stünitz, H., 1993. Deformation of granitoids at low metamorphic
786 grade. I: Reactions and grain size reduction. *Tectonophysics* 221, 269–297.
787 [https://doi.org/10.1016/0040-1951\(93\)90163-E](https://doi.org/10.1016/0040-1951(93)90163-E)

788 Fusses, F., Handy, M.R., 2008. Micromechanisms of shear zone propagation at
789 the brittle–viscous transition. *Journal of Structural Geology* 30, 1242–1253.
790 <https://doi.org/10.1016/j.jsg.2008.06.005>

791 Getsinger, A.J., Hirth, G., 2014. Amphibole fabric formation during diffusion creep
792 and the rheology of shear zones. *Geology* 42, 535–538.
793 <https://doi.org/10.1130/G35327.1>

794 Goleby, B.R., Blewett, R.S., Korsch, R.J., Champion, D.C., Cassidy, K.F., Jones,
795 L.E.A., Groenewald, P.B., Henson, P., 2004. Deep seismic reflection profiling
796 in the Archaean northeastern Yilgarn Craton, Western Australia: implications
797 for crustal architecture and mineral potential. *Tectonophysics* 388, 119–133.
798 <https://doi.org/10.1016/j.tecto.2004.04.032>

799 Goncalves, P., Poilvet, J.C., Olliot, E., Trap, P., Marquer, D., 2016. How does
800 shear zone nucleate? An example from the Suretta nappe (Swiss Eastern
801 Alps). *Journal of Structural Geology* 86, 166–180.
802 <https://doi.org/10.1016/j.jsg.2016.02.015>

803 Goscombe, B.D., Passchier, C.W., 2003. Asymmetric boudins as shear sense
804 indicators—an assessment from field data. *Journal of Structural Geology* 25,
805 575–589. [https://doi.org/10.1016/S0191-8141\(02\)00045-7](https://doi.org/10.1016/S0191-8141(02)00045-7)

806 Griffith, W.A., Rosakis, A., Pollard, D.D., Ko, C.W., 2009. Dynamic rupture
807 experiments elucidate tensile crack development during propagating
808 earthquake ruptures. *Geology* 37, 795–798.
809 <https://doi.org/10.1130/G30064A.1>

810 Guermani, A., Pennacchioni, G., 1998. Brittle precursors of plastic deformation in
811 a granite: an example from the Mont Blanc massif (Helvetic, western Alps).
812 *Journal of Structural Geology* 20, 135–148. [https://doi.org/10.1016/S0191-](https://doi.org/10.1016/S0191-8141(97)00080-1)
813 [8141\(97\)00080-1](https://doi.org/10.1016/S0191-8141(97)00080-1)

814 Handy, M.R., 1990. The solid-state flow of polymineralic rocks. *Journal of*
815 *Geophysical Research* 95, 8647–8661.
816 <https://doi.org/10.1029/JB095iB06p08647>

817 Hobbs, B., Mühlhaus, H., Ord, A., 1990. Instability, softening and localization of
818 deformation. *Geological Society, London, Special Publications* 54, 143–165.

819 Jaquet, Y., Schmalholz, S.M., 2017. Spontaneous ductile crustal shear zone
820 formation by thermal softening and related stress, temperature and strain rate
821 evolution. *Tectonophysics*. <https://doi.org/10.1016/j.tecto.2017.01.012>

822 Jiang, D., White, J.C., 1995. Kinematics of rock flow and the interpretation of
823 geological structures, with particular reference to shear zones. *Journal of*
824 *Structural Geology* 17, 1249–1265. [https://doi.org/10.1016/0191-](https://doi.org/10.1016/0191-8141(95)00026-A)
825 [8141\(95\)00026-A](https://doi.org/10.1016/0191-8141(95)00026-A)

826 Kelemen, P.B., Hirth, G., 2007. A periodic shear-heating mechanism for
827 intermediate-depth earthquakes in the mantle. *Nature* 446, 787–790.
828 <https://doi.org/10.1038/nature05717>

829 Kilian, R., Heilbronner, R., Stünitz, H., 2011. Quartz grain size reduction in a
830 granitoid rock and the transition from dislocation to diffusion creep. *Journal of*
831 *Structural Geology* 33, 1265–1284. <https://doi.org/10.1016/j.jsg.2011.05.004>

832 Kretz, R., 1983. Symbols for rock-forming minerals. *American Mineralogist* 68,
833 277–279.

834 Law, R.D., 2014. Deformation thermometry based on quartz c-axis fabrics and
835 recrystallization microstructures: A review., *Journal of Structural Geology*.
836 <https://doi.org/10.1016/j.jsg.2014.05.023>

837 Lister, G., Snoke, A., 1984. S-C Mylonites. *Journal of Structural Geology* 6, 617–
838 638. [https://doi.org/10.1016/0191-8141\(84\)90001-4](https://doi.org/10.1016/0191-8141(84)90001-4)

839 Mancktelow, N.S., 2002. Finite-element modelling of shear zone development in

840 viscoelastic materials and its implications for localisation of partial melting.
841 Journal of Structural Geology 24, 1045–1053. <https://doi.org/10.1016/S0191->
842 8141(01)00090-6

843 Mancktelow, N.S., Pennacchioni, G., 2005. The control of precursor brittle fracture
844 and fluid–rock interaction on the development of single and paired ductile
845 shear zones. Journal of Structural Geology 27, 645–661.
846 <https://doi.org/10.1016/j.jsg.2004.12.001>

847 Menegon, L., Fousseis, F., Stunitz, H., Xiao, X., 2015. Creep cavitation bands
848 control porosity and fluid flow in lower crustal shear zones. Geology 43, 227–
849 230. <https://doi.org/10.1130/G36307.1>

850 Menegon, L., Pennacchioni, G., 2010. Local shear zone pattern and bulk
851 deformation in the Gran Paradiso metagranite (NW Italian Alps). International
852 Journal of Earth Sciences 99, 1805–1825. <https://doi.org/10.1007/s00531->
853 009-0485-6

854 Myers, J.S., 1995. The generation and assembly of an Archaean supercontinent:
855 evidence from the Yilgarn craton, Western Australia. Geological Society,
856 London, Special Publications 95, 143–154.
857 <https://doi.org/10.1144/GSL.SP.1995.095.01.09>

858 Negrini, M., Stunitz, H., Nasipuri, P., Menegon, L., Morales, L.F.G., 2014.
859 Semibrittle deformation and partial melting of perthitic K-feldspar: An
860 experimental study. Journal of Geophysical Research: Solid Earth 119,
861 3478–3502. <https://doi.org/10.1002/2013JB010573>

862 Pennacchioni, G., Mancktelow, N., 2007. Nucleation and initial growth of a shear
863 zone network within compositionally and structurally heterogeneous
864 granitoids under amphibolite facies conditions. Journal of Structural Geology
865 29, 1757–1780.

866 Pennacchioni, G., Zucchi, E., 2013. High temperature fracturing and ductile
867 deformation during cooling of a pluton: The Lake Edison granodiorite (Sierra
868 Nevada batholith, California). Journal of Structural Geology 50, 54–81.
869 <https://doi.org/10.1016/j.jsg.2012.06.001>

870 Peternell, M., Hasalová, P., Wilson, C.J.L., Piazzolo, S., Schulmann, K., 2010.
871 Evaluating quartz crystallographic preferred orientations and the role of
872 deformation partitioning using EBSD and fabric analyser techniques. Journal
873 of Structural Geology 32, 803–817.

874 Peternell, M., Kohlmann, F., Wilson, C.J.L.C., Seiler, C., Gleadow, A.J.W., 2009.
875 A new approach to crystallographic orientation measurement for apatite
876 fission track analysis: effects of crystal morphology and implications for
877 automation. *Chemical Geology* 265, 527–539.
878 <https://doi.org/10.1016/j.chemgeo.2009.05.021>

879 Platt, J.P., 2015. Influence of shear heating on microstructurally defined plate
880 boundary shear zones. *Journal of Structural Geology* 79, 80–89.
881 <https://doi.org/10.1016/j.jsg.2015.07.009>

882 Prior, D.J., Boyle, A.P., Brenker, F., Cheadle, M.C., Day, A., Lopez, G., Peruzzi,
883 L., Potts, G., Reddy, S., Spiess, R., Timms, N.E., Trimby, P., Wheeler, J.,
884 Zetterstrom, L., 1999. The application of electron backscatter diffraction and
885 orientation contrast imaging in the SEM to textural problems in rocks.
886 *American Mineralogist* 84, 1741–1759. [https://doi.org/10.2138/am-1999-11-](https://doi.org/10.2138/am-1999-11-1204)
887 [1204](https://doi.org/10.2138/am-1999-11-1204)

888 Rowe, C.D., Griffith, W.A., 2015. Do faults preserve a record of seismic slip: A
889 second opinion. *Journal of Structural Geology* 78, 1–26.
890 <https://doi.org/10.1016/j.jsg.2015.06.006>

891 Rowe, C.D., Kirkpatrick, J.D., Brodsky, E.E., 2012. Fault rock injections record
892 paleo-earthquakes. *Earth and Planetary Science Letters* 335–336, 154–166.
893 <https://doi.org/10.1016/j.epsl.2012.04.015>

894 Shigematsu, N., Fujimoto, K., Ohtani, T., Goto, K., 2004. Ductile fracture of fine-
895 grained plagioclase in the brittle–plastic transition regime: implication for
896 earthquake source nucleation. *Earth and Planetary Science Letters* 222,
897 1007–1022. <https://doi.org/10.1016/j.epsl.2004.04.001>

898 Sibson, R.H., 1975. Generation of pseudotachylyte by ancient seismic faulting.
899 *Geophysical Journal International* 43, 775–794.

900 Simpson, C., 1985. Deformation of granitic rocks across the brittle-ductile
901 transition. *Journal of Structural Geology* 7, 503–511.
902 [https://doi.org/10.1016/0191-8141\(85\)90023-9](https://doi.org/10.1016/0191-8141(85)90023-9)

903 Stewart, C.A., Miranda, E.A., 2017. The Rheological Evolution of Brittle-Ductile
904 Transition Rocks During the Earthquake Cycle: Evidence for a Ductile
905 Precursor to Pseudotachylyte in an Extensional Fault System, South
906 Mountains, Arizona. *Journal of Geophysical Research: Solid Earth*.
907 <https://doi.org/10.1002/2017JB014680>

908 Swanson, M.T., 1988. Pseudotachylyte-bearing strike-slip duplex structures in the
909 Fort Foster Brittle Zone, S. Maine. *Journal of Structural Geology* 10, 813–
910 828. [https://doi.org/10.1016/0191-8141\(88\)90097-1](https://doi.org/10.1016/0191-8141(88)90097-1)

911 Tchalenko, J.S., Ambraseys, N.N., 1970. Structural Analysis of the Dasht-e Bayaz
912 (Iran) Earthquake Fractures. *Geological Society of America Bulletin* 81, 41.
913 [https://doi.org/10.1130/0016-7606\(1970\)81\[41:SAOTDB\]2.0.CO;2](https://doi.org/10.1130/0016-7606(1970)81[41:SAOTDB]2.0.CO;2)

914 Thielmann, M., Kaus, B.J.P., 2012. Shear heating induced lithospheric-scale
915 localization: Does it result in subduction? *Earth and Planetary Science Letters*
916 359–360, 1–13. <https://doi.org/10.1016/j.epsl.2012.10.002>

917 Viegas, G., Menegon, L., Archanjo, C., 2016. Brittle grain-size reduction of
918 feldspar, phase mixing and strain localization in granitoids at mid-crustal
919 conditions (Pernambuco shear zone, NE Brazil). *Solid Earth* 7, 375–396.
920 <https://doi.org/10.5194/se-7-375-2016>

921 Wehrens, P., Berger, A., Peters, M., Spillmann, T., Herwegh, M., 2016.
922 Deformation at the frictional-viscous transition: Evidence for cycles of fluid-
923 assisted embrittlement and ductile deformation in the granitoid crust.
924 *Tectonophysics* 693, 66–84. <https://doi.org/10.1016/j.tecto.2016.10.022>

925 Weinberg, R.F., Regenauer-Lieb, K., 2010. Ductile fractures and magma
926 migration from source. *Geology* 38, 363–366.

927 White, J.C., 2012. Paradoxical pseudotachylyte - Fault melt outside the
928 seismogenic zone. *Journal of Structural Geology* 38, 11–20.
929 <https://doi.org/10.1016/j.jsg.2011.11.016>

930 White, J.C., 2005. Transient Creep and Mechanical Instabilities in the Lower
931 Crust: the Long and the Short of It All. AGU Fall Meeting Abstracts.

932 White, J.C., 2004. Instability and localization of deformation in lower crust
933 granulites, Minas fault zone, Nova Scotia, Canada. Geological Society,
934 London, Special Publications 224, 25–37.
935 <https://doi.org/10.1144/GSL.SP.2004.224.01.03>

936 White, J.C., 2003. Windows of Transient Creep and Rupture in Continental
937 Lithosphere. AGU Fall Meeting Abstracts.

938 White, J.C., 1996. Transient discontinuities revisited: pseudotachylyte, plastic
939 instability and the influence of low pore fluid pressure on deformation
940 processes in the mid-crust. *Journal of Structural Geology* 18, 1471–1486.
941 [https://doi.org/10.1016/S0191-8141\(96\)00059-4](https://doi.org/10.1016/S0191-8141(96)00059-4)

- 942 White, S.H., Burrows, S.E., Carreras, J., 1980. On mylonites in ductile shear
943 zones. *Journal of Structural Geology* 2, 175–187.
- 944 Wilde, S.A., Middleton, M.F., Evans, B.J., 1996. Terrane accretion in the
945 southwestern Yilgarn Craton: evidence from a deep seismic crustal profile.
946 *Precambrian Research* 78, 179–196.
- 947 Wyche, S., Ivanic, T., Zibra, I., 2013. Youanmi and Southern Carnarvon seismic
948 and magnetotelluric (MT) workshop 2013. Geological Survey of Western
949 Australia, Record 6, 180 p. Available at:
950 [http://dmpbookshop.eruditetechnologies.com.au/product/youanmi-and-](http://dmpbookshop.eruditetechnologies.com.au/product/youanmi-and-southern-carnarvon-seismic-and-magnetotelluric-mt-workshop-2013.do)
951 [southern-carnarvon-seismic-and-magnetotelluric-mt-workshop-2013.do](http://dmpbookshop.eruditetechnologies.com.au/product/youanmi-and-southern-carnarvon-seismic-and-magnetotelluric-mt-workshop-2013.do)
- 952 Wyche, S., Kirkland, C.L., Riganti, A., Pawley, M.J., Belousova, E., Wingate,
953 M.T.D., 2012. Isotopic constraints on stratigraphy in the central and eastern
954 Yilgarn Craton, Western Australia. *Australian Journal of Earth* 59, 657–670.
955 <https://doi.org/10.1080/08120099.2012.697677>
- 956 Zibra, I., Clos, F., Weinberg, R.F., Peternell, M., 2017a. The ~2730 Ma onset of
957 the Neoproterozoic Yilgarn Orogeny. *Tectonics* 36, 1787–1813.
958 <https://doi.org/10.1002/2017TC004562>
- 959 Zibra, I., Gessner, K., Smithies, R.H., Peternell, M., 2014a. On shearing,
960 magmatism and regional deformation in Neoproterozoic granite-greenstone
961 systems: Insights from the Yilgarn Craton. *Journal of Structural Geology* 67,
962 253–267. <https://doi.org/10.1016/j.jsg.2013.11.010>
- 963 Zibra, I., Korhonen, F.J., Peternell, M., Weinberg, R.F., Romano, S.S., Braga, R.,
964 De Paoli, M.C., Roberts, M., 2017b. On thrusting, regional unconformities and
965 exhumation of high-grade greenstones in Neoproterozoic orogens. The case of
966 the Waroonga Shear Zone, Yilgarn Craton. *Tectonophysics* 712–713, 362–
967 395. <https://doi.org/10.1016/j.tecto.2017.05.017>
- 968 Zibra, I., Smithies, R.H., Wingate, M.T.D., Kirkland, C.L., 2014b. Incremental
969 pluton emplacement during inclined transpression. *Tectonophysics* 623, 100–
970 122. <https://doi.org/10.1016/j.tecto.2014.03.020>

971

972 **Figure captions**

973

974 **Fig. 1.** Geological setting of the Cundimurra Shear Zone. (a) Simplified sketch of
975 the Yilgarn Craton showing the subdivision into main terranes, and the
976 location of the studied shear zone (Cundimurra Shear Zone, CMSZ).
977 Terrane nomenclature after Cassidy et al. (2006). EGST: Eastern
978 Goldfields Superterrane. (b) Geological sketch map of the Cundimurra
979 Pluton/Shear Zone. Rectangle shows location of the study area and figure
980 2. "GR" indicates the Garden Rock Monzogranite. (c) Three-dimensional
981 sketch summarizing the main geometric and kinematic features of the
982 Cundimurra Pluton/Shear Zone, as constrained by field and geophysical
983 data. Modified after Zibra et al. (2014b).

984 **Fig. 2.** Geological map of the Lake Austin Shear Zone, showing the spatial
985 distribution of the main structural domains. Inset (a) shows an equal-area
986 projection plot of the solid-state fabric (S_{MT} and L_{MT}) predating the
987 Moyagee fault. For each equal-area projection, within brackets: number of
988 measurements (n) and mean value (symbol). Inset (b) shows the
989 orientation of the main fabric in the Golconda mylonite, postdating the
990 Moyagee fault. Inset (c) shows the orientation of the gneissic foliation and
991 mineral lineation (S_G and L_G , respectively) in host greenstones. Inset (d)
992 shows the distribution of the magmatic foliation within the undeformed, c.
993 2620 Ma Garden Rock Monzogranite, which postdates all the shearing
994 events in the study area.

995 **Fig. 3.** (a) Geological map of the Moyagee fault, showing geometric relations
996 between the western pluton boundary, the steeply-dipping S_{MT} and the fault
997 network. (b) Sketch illustrating an ideal fault array in a dextral, synthetic
998 driven Riedel shear zone. Modified after Ahlgren (2001). (c) and (d) show
999 the two equal-area stereographic projections for orientations of main
1000 structural elements. In (c), S_U and L_U refer to cataclasite-derived
1001 ultramylonites. In (d), S_{CAT} and L_{CAT} refer to foliation and lineation (the latter
1002 indicated by slickensides) in undeformed cataclasites, respectively. S_{OBL}
1003 and L_{OBL} refer to fault segments at high angle from the main fault surfaces.
1004 Symbols near the number of measurements indicate mean values.

1005 **Fig. 4.** Detailed maps of the Moyagee fault, obtained by a combination of
1006 orthophoto observations and conventional structural mapping. Fig. 4. (a)
1007 The Moyagee fault is an array of left-stepping en-echelon fault segments
1008 with R-type orientation (red) relative to the western boundary of the
1009 Cundimurra Pluton. Shorter faults with P-type orientation (red) link the en
1010 echelon segments. (b) Detailed fault map shows the fault network
1011 configuration to be consistent across several orders of magnitude. (c) Map
1012 of a complex brittle fault segment comprised of parallel fault traces with cm-
1013 scaling spacing and minimal ductile overprint. The fault segment terminates
1014 southward in an array of small, horse-tailing reverse faults. (d) Histograms
1015 of orientation data of veins for the Moyagee fault, including all data from
1016 undeformed cataclasites and cataclasite-derived ultramytonites.

1017 **Fig. 5.** (a) Horizontal pavement as an image and interpreted drawing showing a
1018 representative example of paired fault surfaces, developed along the
1019 contact between a gneissic pegmatite and host granitic gneiss. Insets of
1020 equal-area plots show orientation of the mylonitic foliation and lineation at
1021 each locality. Inset at lower right sketches the main types of Riedel shears
1022 observed in this outcrop. Main Y-shears are ~50 cm apart, connected by
1023 synthetic R-shears. Along the lithological boundary, granitic gneiss
1024 contains a dense network of shear surfaces sub-parallel to the main Y-
1025 shear. Figures (b) – (f) show detailed outcrop-scale images and maps of
1026 three portions of the fault network shown in Figure 4c, which is devoid of
1027 any ductile overprint. (b) The domain comprised between the paired faults
1028 developed a dense network of fractures, associated with large volumes of
1029 tourmaline-rich veins. Main Y-shears are associated with high-angle T-
1030 fractures and are joined by synthetic R-shears. In foliated domains, the
1031 overall sigmoidal shape of clasts, or clast aggregates, is in agreement with
1032 the dominant dextral shear sense. (c) Close-up view of the planar, central
1033 part of (b) showing an array of nearly evenly-spaced, tourmaline-filled veins
1034 at high-angle to the fault surface. (d) Detail of well-developed antithetic R'-
1035 shears. Y-, R- and R'-shears, all nearly subvertical. (e) Complex fracture
1036 network developed within closely spaced, paired fault surfaces, some 10 m
1037 north from the fault network shown in (b). (f) The northernmost exposed

1038 segment of this fault network shows two main paired surfaces, ~1.5 m
1039 apart, joined by partially developed synthetic R-shears. While the overall
1040 fracture geometry in this segment is similar to the one shown in (b), in this
1041 case the volume of tourmaline-rich veins is notably smaller. (g) Close-up
1042 view of a ~20 cm-thick mylonite zone developed along the lithological
1043 contact between a composite aplite-pegmatite vein and host granitic
1044 gneiss, from a 2 km-long, tourmaline-free fault segment, located at the
1045 southern end of the Moyagee fault (Fig. 3a). Note that pinch-and-swell
1046 structure occurs in the pegmatite layer only. Within the mylonite, S–C and
1047 C' subfabrics, together with sigmoidal feldspar porphyroclasts, indicate
1048 dextral shear sense. Protomylonitic granite flanking the northeastern side
1049 of the shear zone preserves a network of fractures and small-scale faults,
1050 suggesting that the mylonite developed at the expenses of a pre-existing
1051 cataclasite. Inset of equal-area plot shows orientation of the mylonitic
1052 foliation and lineation at this locality. (h) Representative example of
1053 “pseudotachylyte-like” fault surface, developed within an aplite vein. The
1054 vein is ~2 cm-thick, it contains a small proportion of clasts from host
1055 gneiss, and it is associated with cm-thick lateral veins resembling injection
1056 veins in pseudotachylytes. The trace of S_{MT} is highlighted by aligned mica
1057 flakes.

1058 **Fig. 6.** (a) Horizontal exposure of a paired cataclasite-ultramylonite. The eastern
1059 side of this composite structure largely preserves outcrop-scale features
1060 recorded during cataclasite development, including randomly-oriented clast
1061 from host gneiss and high-angle, undeformed T-fractures with sub-
1062 millimetric thickness (arrowheads). In contrast, the western side of the vein
1063 contains a layered ultramylonite, derived from ductile deformation of
1064 cataclasite. Note the abrupt transition between weakly-deformed
1065 cataclasite and ultramylonite, marked by the yellow dashed line. Inset of
1066 equal-area plot shows orientation of the mylonitic foliation and lineation at
1067 this locality. (b) Polished hand sample (212727) from a paired cataclasite-
1068 ultramylonite. The ultramylonite developed at the expenses of cm-thick
1069 cataclasite, which is locally preserved along strike. Veins developed near
1070 the main rupture surface and pre-existing S_{MT} in the host were ductilely

1071 deformed and rotated into parallelism with the ultramylonite. On the eastern
1072 side of the main surface, high-angle T surfaces are virtually undeformed,
1073 except for the region marked by (*), where mm-long segments of T veins
1074 were dextrally dragged into the ultramylonite. Microstructures from this
1075 sample are described in section 4.

1076 **Fig. 7.** The role of lithological contacts in strain localization. **Fig. 3** for photograph
1077 location. (a) Layered granitic gneiss at margins of the Moyagee fault, with
1078 aplites and pegmatites subparallel to S_{MT} . (b) Tourmaline-bearing
1079 cataclasite developed along the contact between an aplite vein and host
1080 granitic gneiss. White arrowhead points to a T-fracture whose orientation
1081 indicates dextral shear sense. Black arrowhead points to an isoclinally
1082 folded T-fracture, in the mylonitized portion of the aplite vein. Scale bar at
1083 lower right, in both (a) and (b), is 5 cm-long (c) Tourmaline-bearing
1084 ultramylonite developed along the contact between a gneissic pegmatite
1085 and host granitic gneiss. Internal layering in ultramylonite is likely due to
1086 sheared cataclasite clasts (compare with **Fig. 6**, from the same fault
1087 segment). Pencil for scale. (d) Tourmaline-bearing, layered ultramylonites
1088 developed along both lithological contacts between a gneissic pegmatite
1089 and host granitic gneiss. Along the lower contact, C shear bands in
1090 pegmatite indicate dextral shear sense, which is highlighted with a line
1091 drawing. (e) Shearband boudins developed in a sheared pegmatite near
1092 the margins of the Moyagee fault. Boudinage occurred along knife-sharp,
1093 synthetic shears that only developed near the pegmatite. Pen for scale. (f)
1094 Detail from a sigmoid-shaped boudin block bounded by shear bands. (g)
1095 Shear zone localized in aplite vein, showing ~1m of dextral displacement
1096 and subhorizontal stretching lineation (L_U), with line drawing in lower left to
1097 illustrate features and show the position of Figure 7h. Scale bar at lower
1098 right is 2 cm-long (h) Detail from (g) showing the knife-sharp transition
1099 between the sheared aplite and S_{MT} in host gneiss.

1100 **Fig. 8.** (a) Geological map of the Pinnacles Domain, i.e. the northernmost
1101 segment of the Lake Austin Shear Zone. Inset of equal-area projection plot
1102 shows lineations and poles to foliation for both granitic gneiss and

1103 greenstones. (b) Detail from a boudinaged granitic dyke, previously
1104 intruded into ultramafic schists ((a) shows location). Tourmaline-injected
1105 cataclasite developed along the contact between the granitic dyke and the
1106 quartz vein with both lithologies occurring as angular clasts in the
1107 cataclasite. (c) Detail from the same boudinaged granitic dyke shown in (b),
1108 here preserving a more a more advanced stage of brecciation with angular
1109 clasts deriving from the granite dyke and the adjacent, late-magmatic
1110 quartz vein. (d) Representative microstructure of tourmaline-rich veins
1111 associated with cataclasite in a boudinaged, mylonitic granite dyke. The
1112 vein recorded domino-type boudinage whose asymmetry indicating dextral
1113 shear sense, consistently with sigmoidal K-feldspar porphyroclasts
1114 (arrowhead). The granitic dyke shows a mylonitic foliation that predates
1115 boudinage and predates the emplacement of the tourmaline vein itself.
1116 Cross-polarized light.

1117 **Fig. 9.** Main mesoscale features in the Golconda mylonite. (a) Horizontal
1118 exposure showing the prominent S-C fabric that typifies the Golconda
1119 mylonite. (b) Oblique view on a horizontal exposure showing mylonitic
1120 folds, with axial plane and fold axes sub-parallel to S_U and L_U , respectively.
1121 S_U is folded, indicating that these folds developed late in the shearing
1122 history. Closely-spaced ultramylonites likely nucleated on paired
1123 cataclasites (i.e. compare with [figs 5a–f](#)). (c) Horizontal (i.e. near XZ)
1124 exposure of a layered ultramylonite, developed at the expense of a former
1125 cataclasite. In the central, blue and white portion, compositional layering is
1126 likely defined by stretched clasts from host gneiss (i.e. compare with [Fig.](#)
1127 [6](#)). In the gneissic portion of the shear zone, S-C fabric and C' shear bands
1128 indicate dextral shear sense. The layering is offset by a network of
1129 antithetic slip surfaces defining domino-type boudinage. Note that, in the
1130 upper part of the layer (in the domains indicated by “*”), mylonitic foliation
1131 is not deflected around offset boudin blocks, indicating that brittle
1132 deformation occurred at a very late stage of shearing. (d) Plurimetric, knife-
1133 sharp fault developed $\sim 10^\circ$ clockwise from the prominent C fabric, whose
1134 trace is indicated by the yellow dashed line. (e) Detail from (d) showing en

1135 echelon fault segments joined by high-angle wing cracks. Linkage occurs
1136 at right-stepping extensional stepovers (f) Sketch showing a model of fault
1137 development as conjugate R- shears and wing cracks (W), in relation to
1138 main slip surfaces, corresponding to the C fabric.

1139 **Fig. 10.** Subfigures (a)–(d): representative pre-cataclasite meso- and
1140 microstructures from granitic gneiss at margins of the Moyagee fault. All
1141 photomicrographs are cross-polarized, unless specified. (a) Polished hand
1142 sample from the contact between boudinaged pegmatite and host granitic
1143 gneiss (compare with Fig. 7f). Note that, in granitic gneiss, most
1144 plagioclase and K-feldspar porphyroclasts show evidence of cataclasis
1145 (one example is indicated by the red arrowhead). (b) high-strain version of
1146 S_{MT} , showing widespread brittle deformation in feldspar and lensoid quartz
1147 ribbons (the latter marked by white arrowheads). Antithetic microfaults in K-
1148 feldspar (yellow arrowhead) and small-scale shear bands (red arrowhead)
1149 indicate dextral shear sense. (c) Close-up view at a strain shadow domain
1150 (outlined by the yellow dashed lines) near a K-feldspar porphyroclast
1151 (“Kfs”). The strain shadow contains elongate aggregates of porphyroclast
1152 fragments, embedded within fine-grained recrystallized feldspar (10–20 μ m
1153 in size). (d) Shear band sharply truncating S_{MT} , along the boundary
1154 between the boudinaged pegmatite and host granitic gneiss. Angular
1155 feldspar fragments preserved at the base of the photo are mantled by fine-
1156 grained recrystallized feldspar, in analogy with what shown in (c).
1157 Subfigures (e) to (h): sample 212762, representative of an undeformed
1158 cataclasite. (e) Hand sample of a “pseudotachylyte-like” injection vein, at
1159 high-angle to S_{MT} in host gneiss. (f) Micrograph from the central portion of
1160 the vein shown in (e), here at moderate angle from S_{MT} in host gneiss. The
1161 vein contains mm-sized tourmaline₁ grains, now replaced by finer-grained
1162 tourmaline₂, and angular to rounded clasts from the host gneiss. Note the
1163 elongate trails of fine-grained recrystallized feldspar in host gneiss
1164 (indicated by the red dashed line), defining the ultramylonite domain
1165 (“Umyl”). Mineral abbreviations after Kretz (1983). All thin sections were
1166 prepared along the XZ sections of the finite strain ellipsoid; that is,
1167 perpendicular to S_{MT} and parallel to L_{MT} in the cataclasite, and

1168 perpendicular to S_U and parallel to L_U for the ultramylonite. (g)
1169 Ultramylonite layer, marked by completely recrystallized feldspar (10–20
1170 μm in size), along the contact between cataclasite and host gneiss. Note
1171 that quartz lenses contain polygonal, apparently strain-free grains.
1172 Ultramylonite is cut by ~ 50 μm -thick cataclasite veins (arrowhead),
1173 branching off the main fault surface. (h) Close-up view from (g), showing
1174 portions of ultramylonite as fragments within the tourmaline-bearing
1175 cataclasite.

1176 **Fig. 11.** Representative microstructures from mylonites and ultramylonites. (a)
1177 Whole-thin section micrograph showing the relationships between P and T
1178 surfaces and the ultramylonite. Compare with Fig. 7. Rectangles show
1179 location of additional micrographs from the same sample. Plane polarized
1180 light. (b) SEM-BSE image of a transposed and mylonitized vein. Note the
1181 shape preferred orientation and the pinch and swell of lensoid quartz
1182 ribbon. (c) Mylonite domain, in a zone of transposed T_1 veins, which are
1183 mainly composed by ultrafine (~ 1 – $10\mu\text{m}$) tourmaline₂ aggregates. Shear
1184 band type feldspar porphyroclasts (near the centre) prevail in this domain.
1185 (d) SEM-BSE image of the ultramylonite microstructure. The image shows
1186 the contact between the granitic ultramylonite on the left side and the
1187 ultramylonite derived from the tourmaline-rich cataclasite on the right side.
1188 (e) EDS-derived compositional maps of part of the ultramylonite
1189 microstructure shown in (d). Note the thin films of K-feldspar filling the
1190 incipient gaps between quartz grains in a polycrystalline quartz ribbon.
1191 Domino-type boudinage in quartz ribbon indicates dextral shear sense.
1192 Note that these maps show the same boudinaged quartz ribbon shown in
1193 the left part of (d). However, the actual frame of (e) is not included in (d). (f)
1194 Pinch-and-swell and boudinage in a one-grain-thick quartz ribbons (central
1195 layer). Boudin neck infill is matrix feldspar (e.g. see the yellow, wedge-
1196 shaped K-feldspar grain near the centre). Gypsum plate inserted. (g) SEM-
1197 BSE image of the ultrafine-grained matrix of the tourmaline-rich
1198 ultramylonite. At left, a boudinaged quartz ribbon shows K-feldspar infill. (h)
1199 Close-up view on compositional layering in the ultramylonite domain. Dark
1200 layers are 10–20 μm -thick and contain euhedral, aligned tourmaline₂

1201 grains. Other tourmaline₂ grains are dispersed in the quartzofeldspathic
1202 polygonal aggregate (white), where average grain size is ~10–20 μm.
1203 Plane polarized light. (i) Festoons of isolated polycrystalline quartz lenses
1204 and opaque aggregates defining C'-type bands in the quartzofeldspathic
1205 ultramylonite matrix.

1206

1207 **Fig 12.** Quartz CPO data from the ultramylonite, obtained by using an automated
1208 fabric analyser microscope (sample 198170) and with EBSD analysis
1209 (sample 212727). (a) Pole figures of quartz grains in polycrystalline
1210 ribbons. For sample 212727, the following crystallographic directions and
1211 poles to planes were plotted: c-axis <0001>, a-axis {11-20}, prism plane
1212 {10-10}, positive rhombohedral plane {10-11}, negative rhombohedral plane
1213 {01-11}. Data are plotted as one point per grain (N = number of grains). In
1214 both samples, the quartz c-axis fabric opening angle, measured across the
1215 Z axis, is about 70–75°. (b) Inverse Pole Figure (IPF) map of tourmaline,
1216 colour-coded with respect to the stretching lineation of the ultramylonite.
1217 The inset shows the IPF of tourmaline. Grain boundaries (misorientation >
1218 10°) are shown in black, low-angle boundaries (misorientation between 2°
1219 and 10°) are shown in cyan. Grey areas represent unindexed points. (c)
1220 Pole figures of the tourmaline grains from the map shown in (b). Plotted
1221 crystallographic directions and poles to planes are: c-axis <0001>, prism
1222 plane {10-10}. Data are plotted as one point per grain (N = number of
1223 grains). In both (a) and (c), maxima are expressed as multiples of the
1224 uniform distribution.

1225

1226 **Fig 13.** (a) Sketch illustrating the inferred transition from dominantly ductile high-
1227 strain zones developed along lithological contacts to cataclasite. Redrawn
1228 after Figs. 5b, 7b, e and f. (b) Idealized sketch showing the early stages of
1229 development of the Lake Austin Shear Zone, with development of the two
1230 main networks of brittle structures (the Moyagee and Pinnacles faults), in
1231 turn overprinted by localized ultramylonites. (c) Further shearing along the
1232 Lake Austin Shear Zone was accommodated by shear zone broadening

1233 with the development of the Golconda mylonite, overprinting brittle and
1234 ductile structures. (d) Equal-area projection plots for each deformation
1235 stage. Note that the kinematic framework developed during the late stages
1236 of pluton emplacement (represented by S_{MT} and L_{MT}) remains unchanged
1237 during the development of the Lake Austin Shear Zone. Symbols near the
1238 number of measurements indicate mean values.

1239

1240

1241

1242

1243

1244

1245

1246

1247

1248

1249

1250

1251

1252

1253

1254

*Figure 1
[Click here to download high resolution image](#)

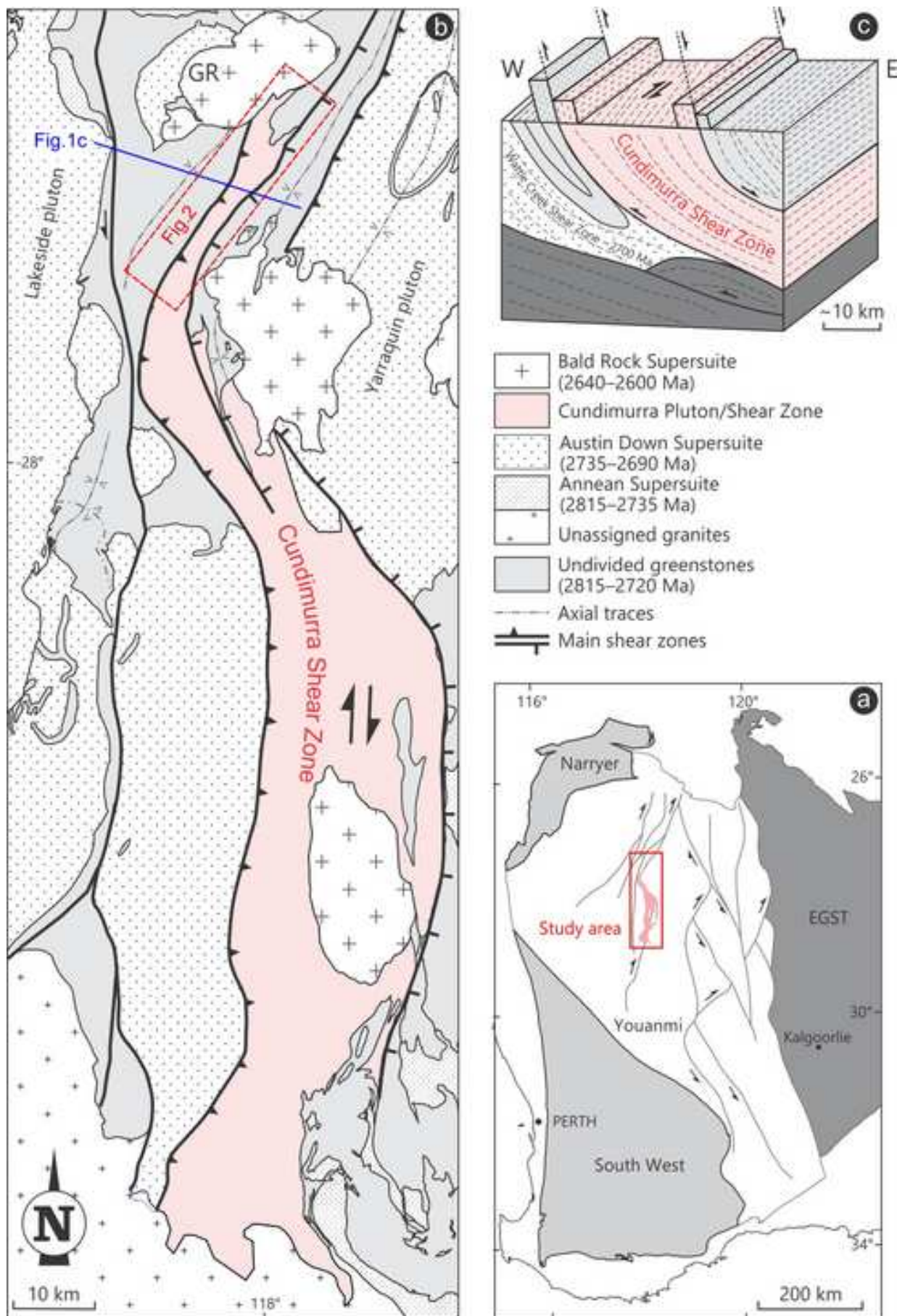


*Figure 2
[Click here to download high resolution image](#)

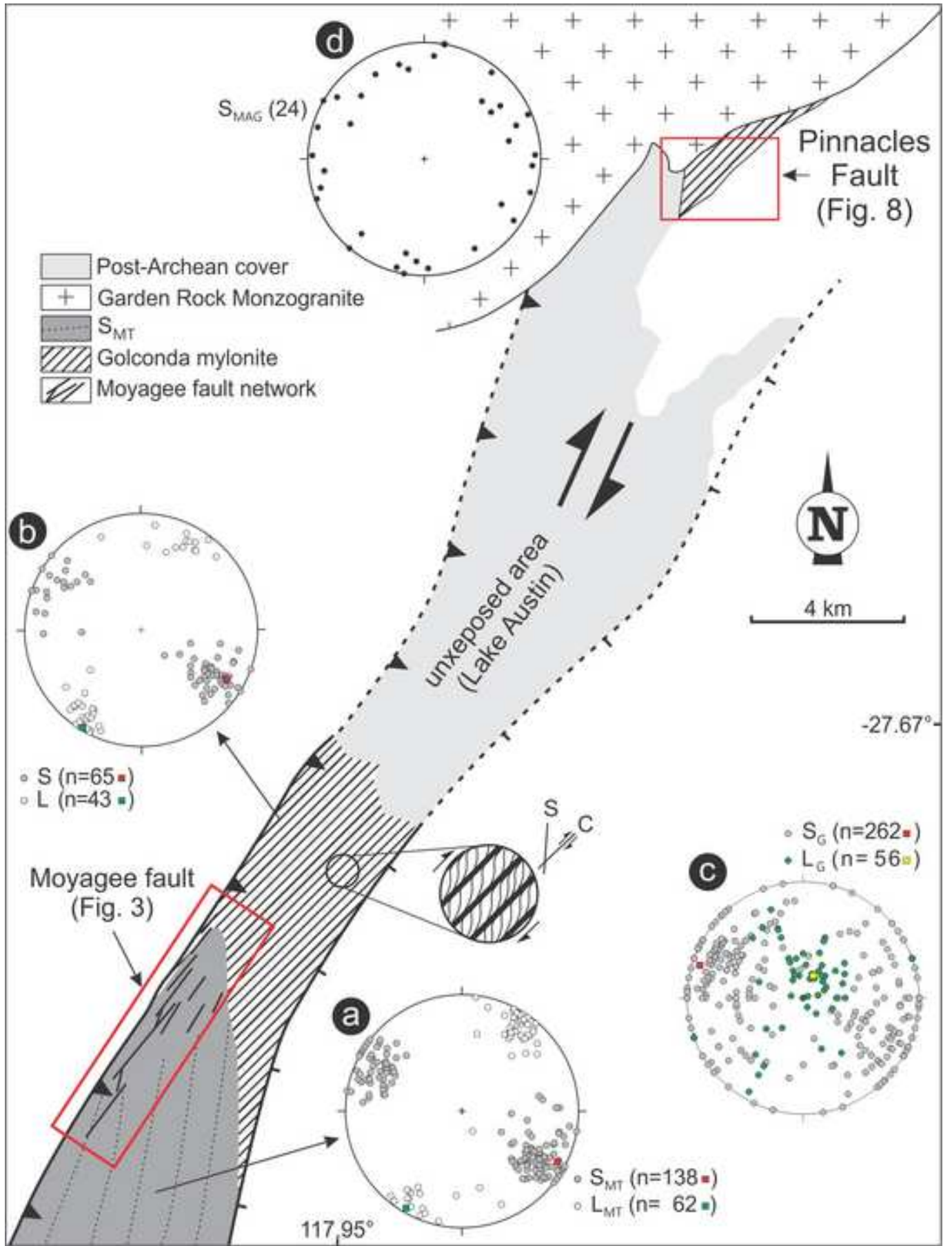


***Figure 3**
[Click here to download high resolution image](#)

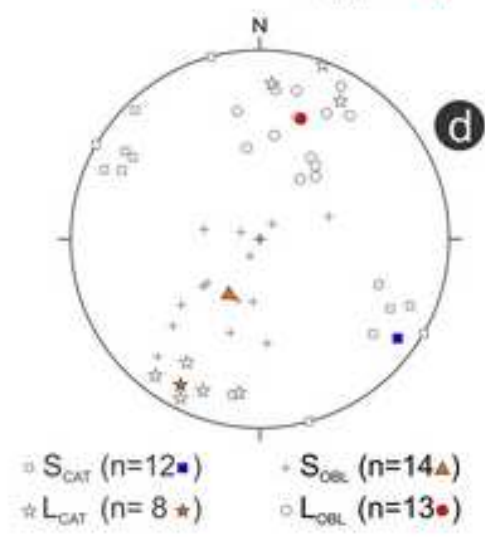
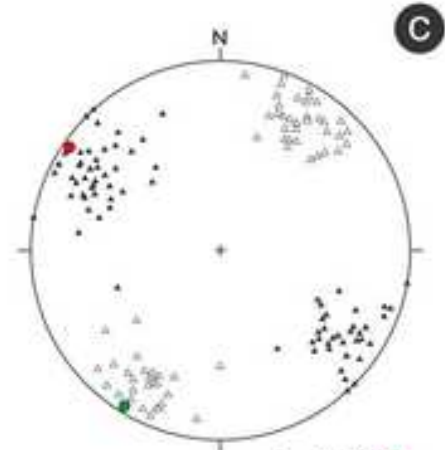
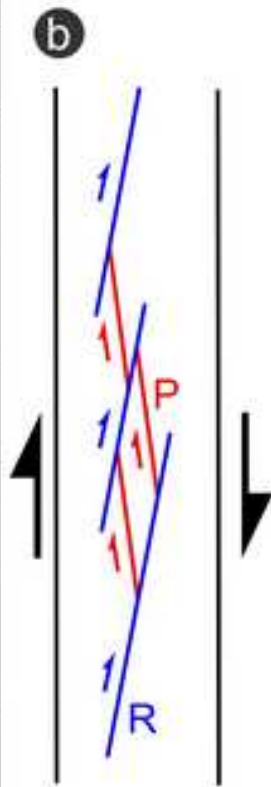
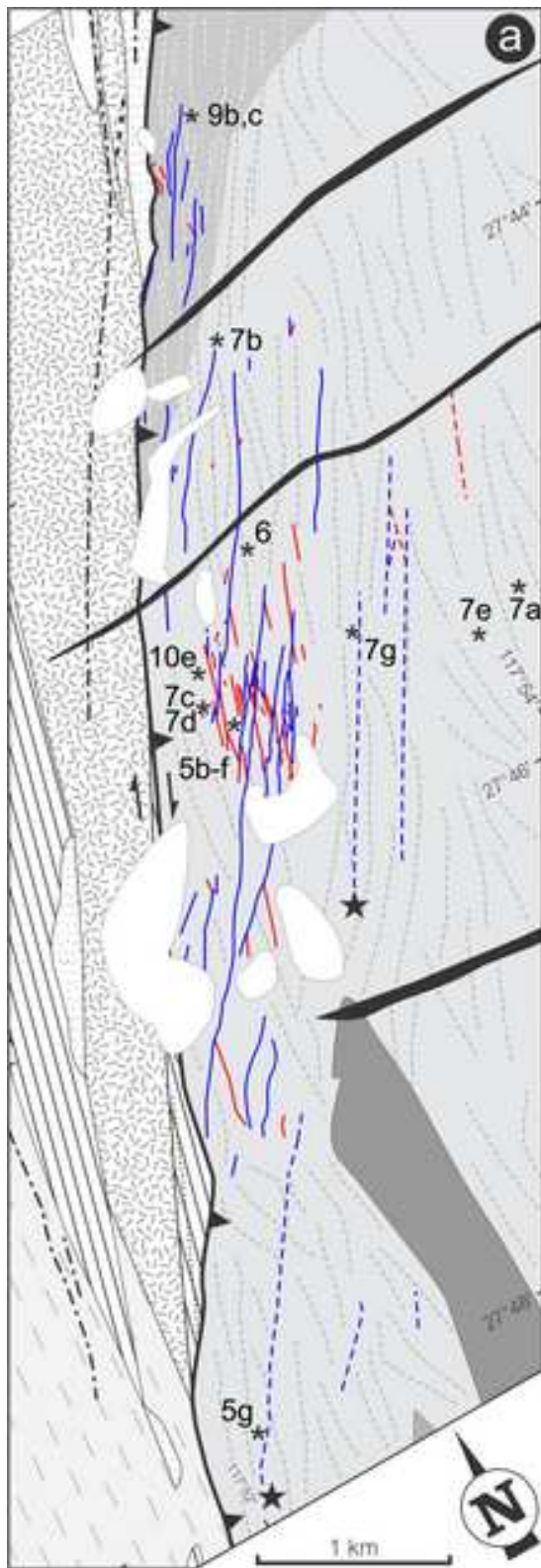


*Figure 4ac

[Click here to download high resolution image](#)

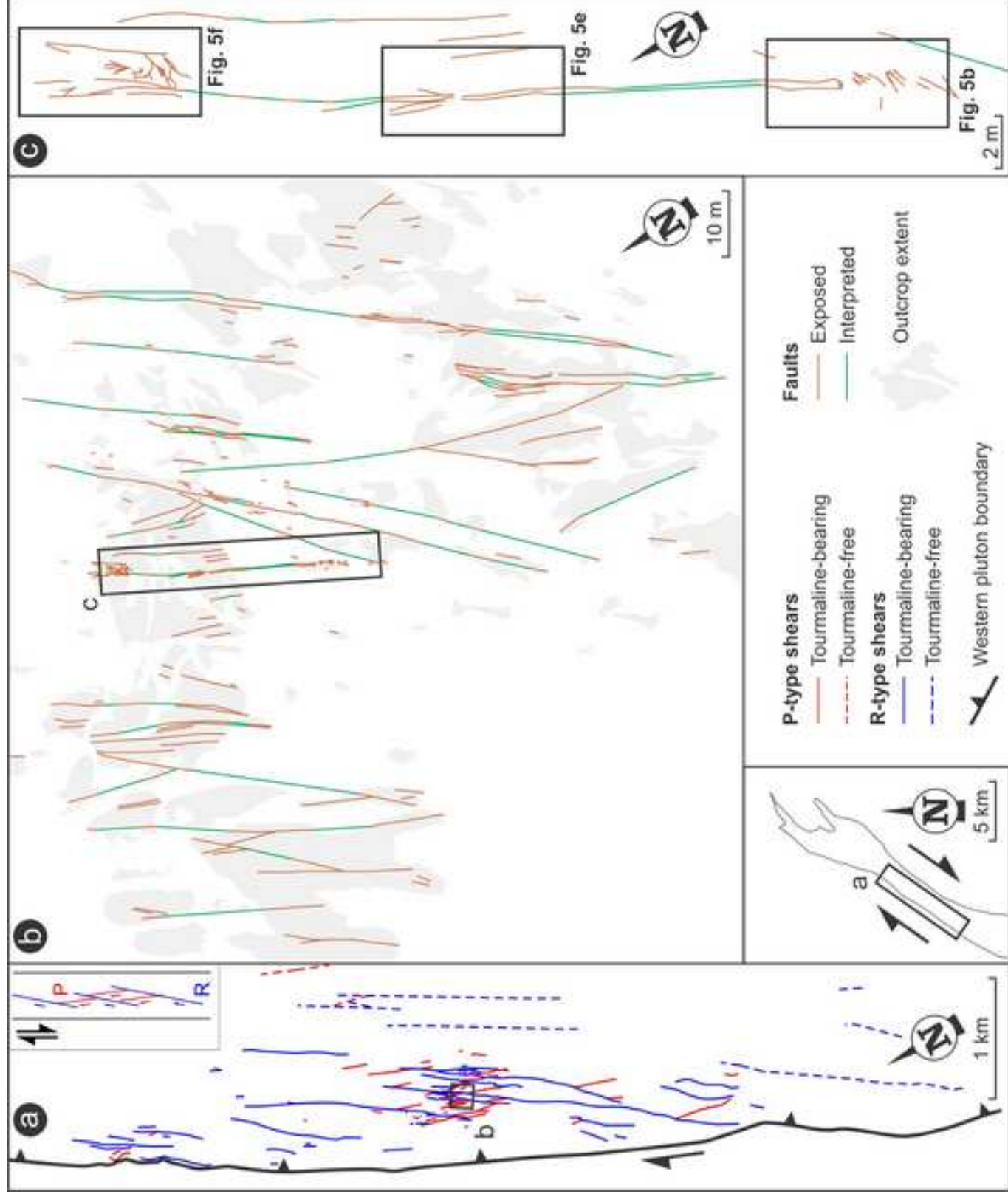


*Figure 4d
[Click here to download high resolution image](#)

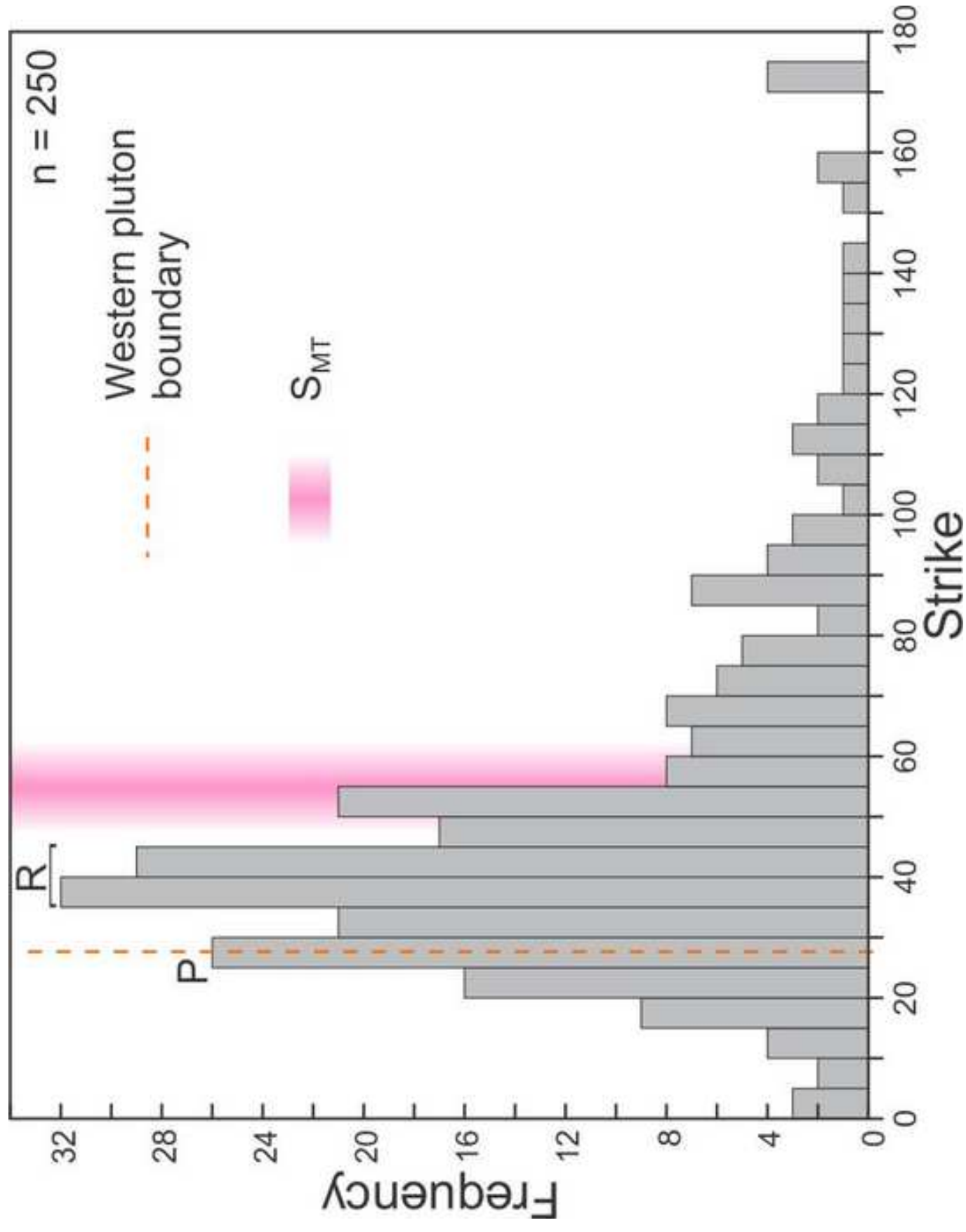


*Figure 5a
[Click here to download high resolution image](#)

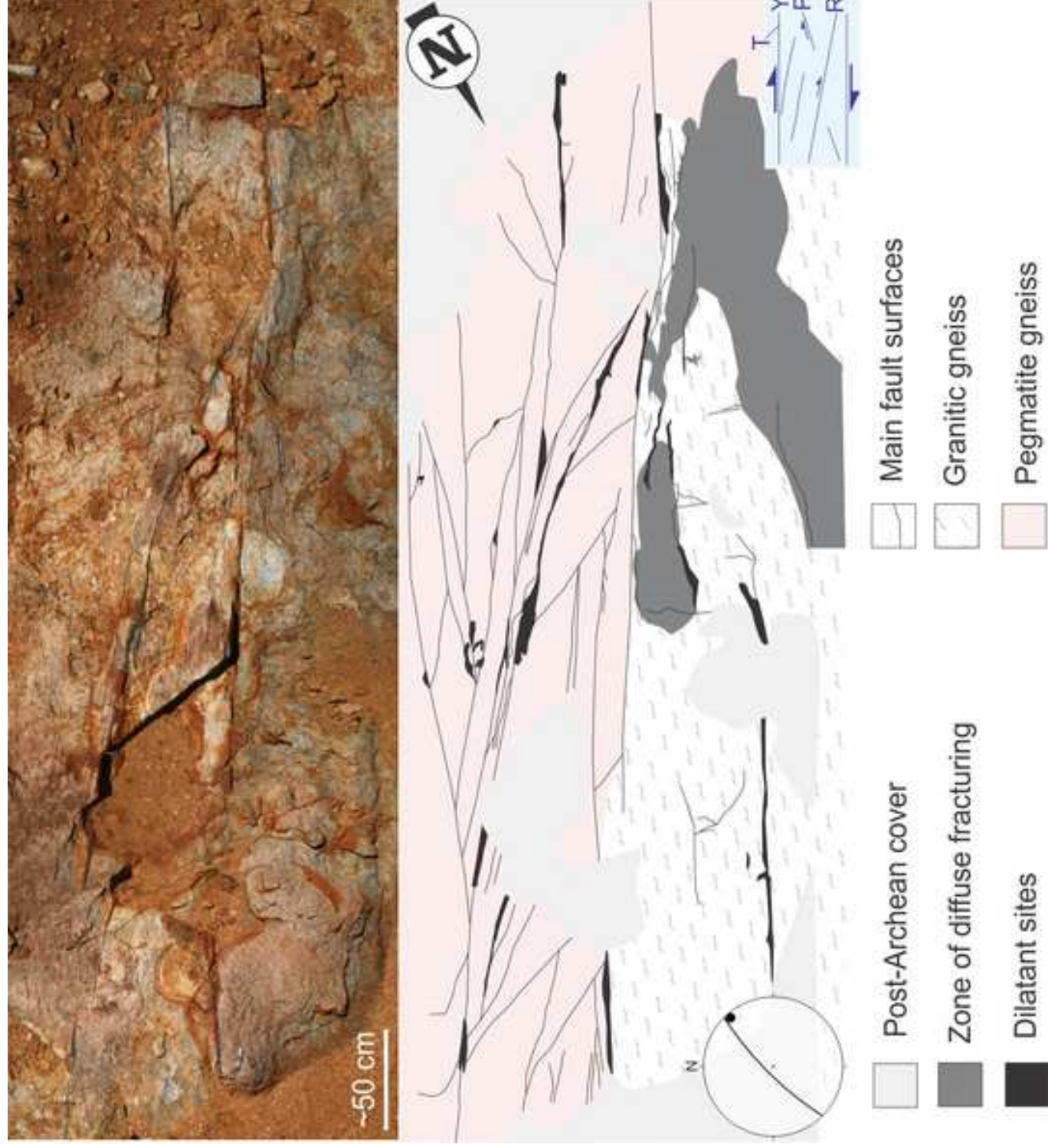


*Figure 5bd

[Click here to download high resolution image](#)

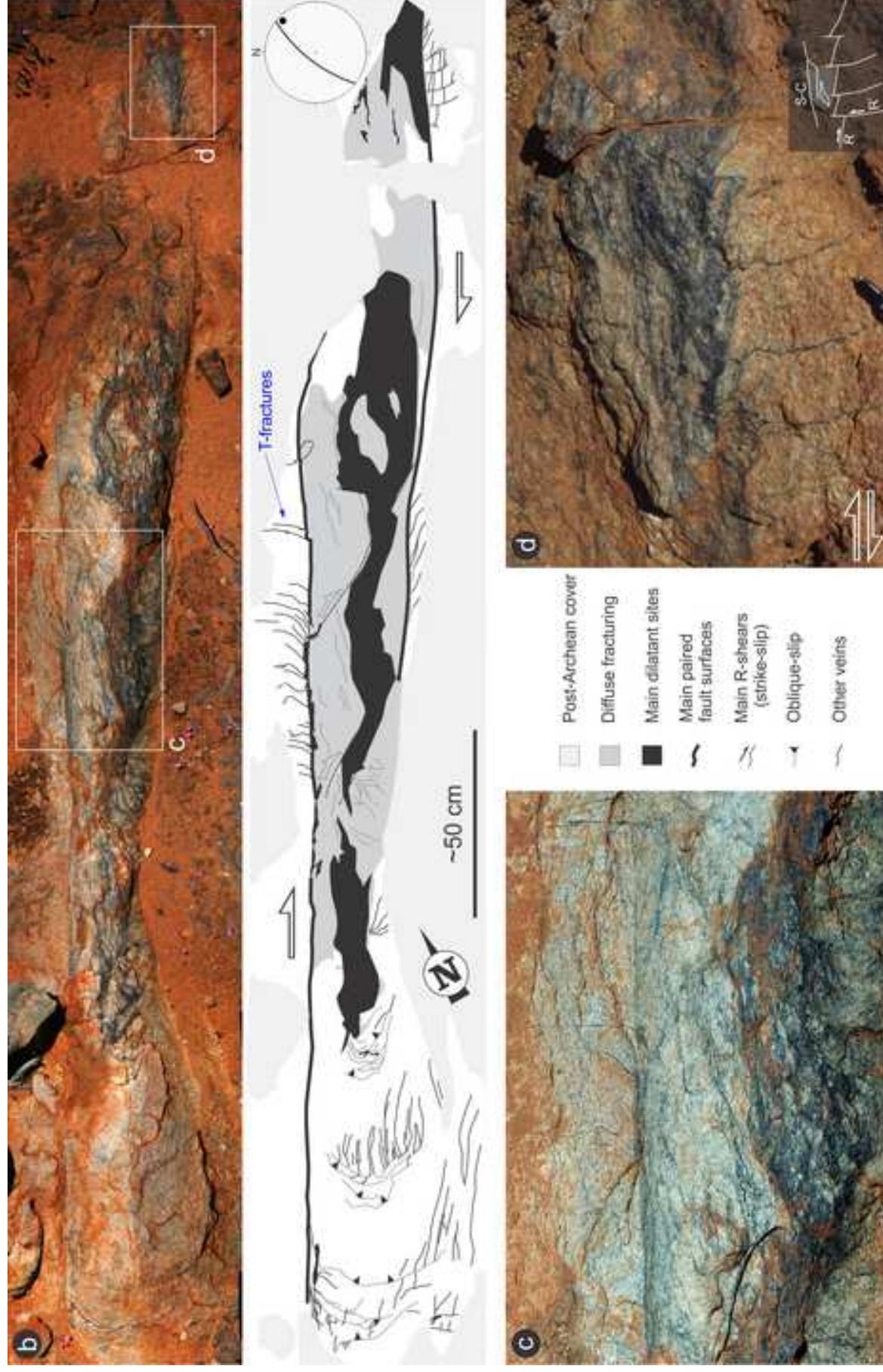


*Figure 5ef
[Click here to download high resolution image](#)

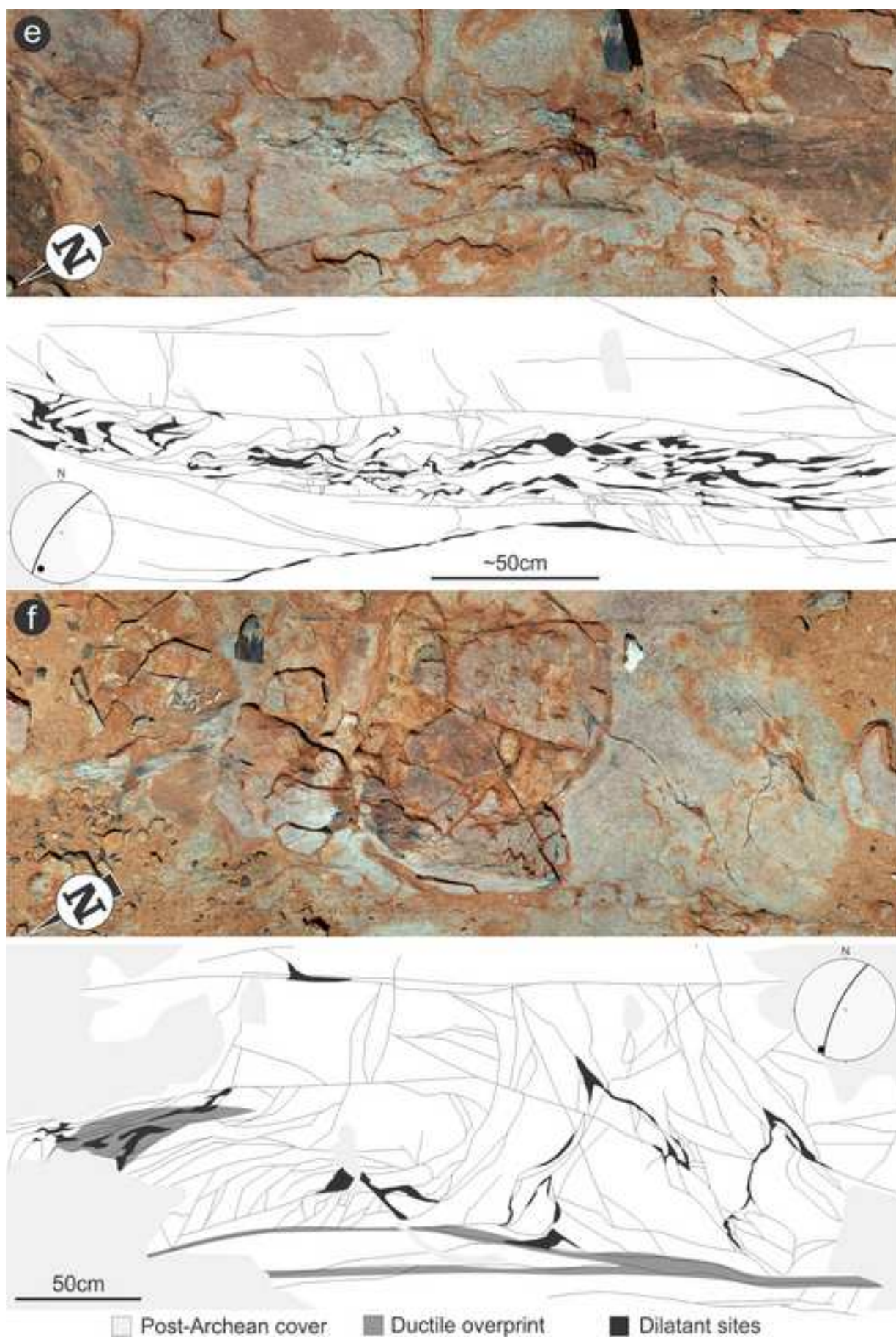


*Figure 5h
[Click here to download high resolution image](#)

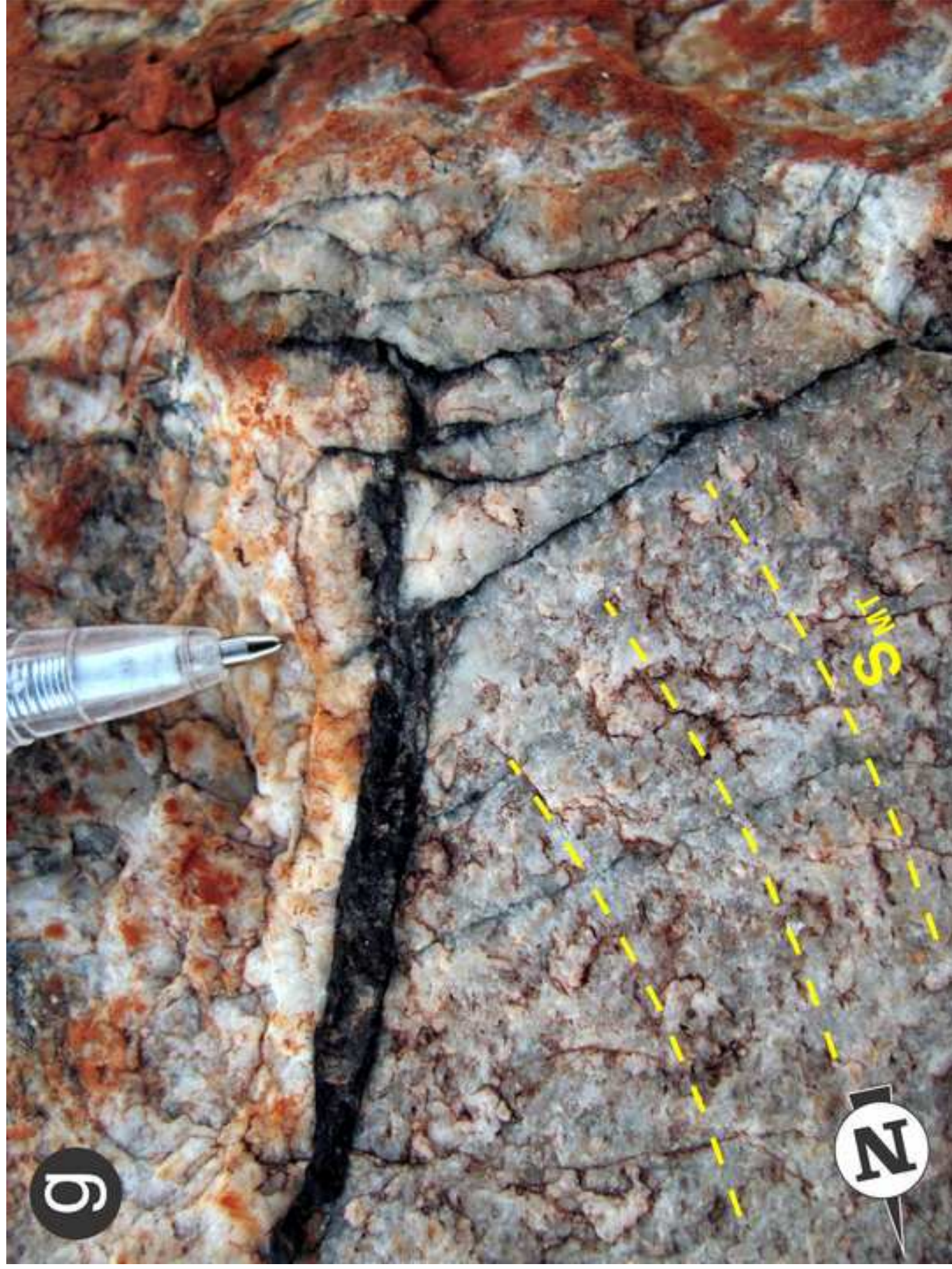
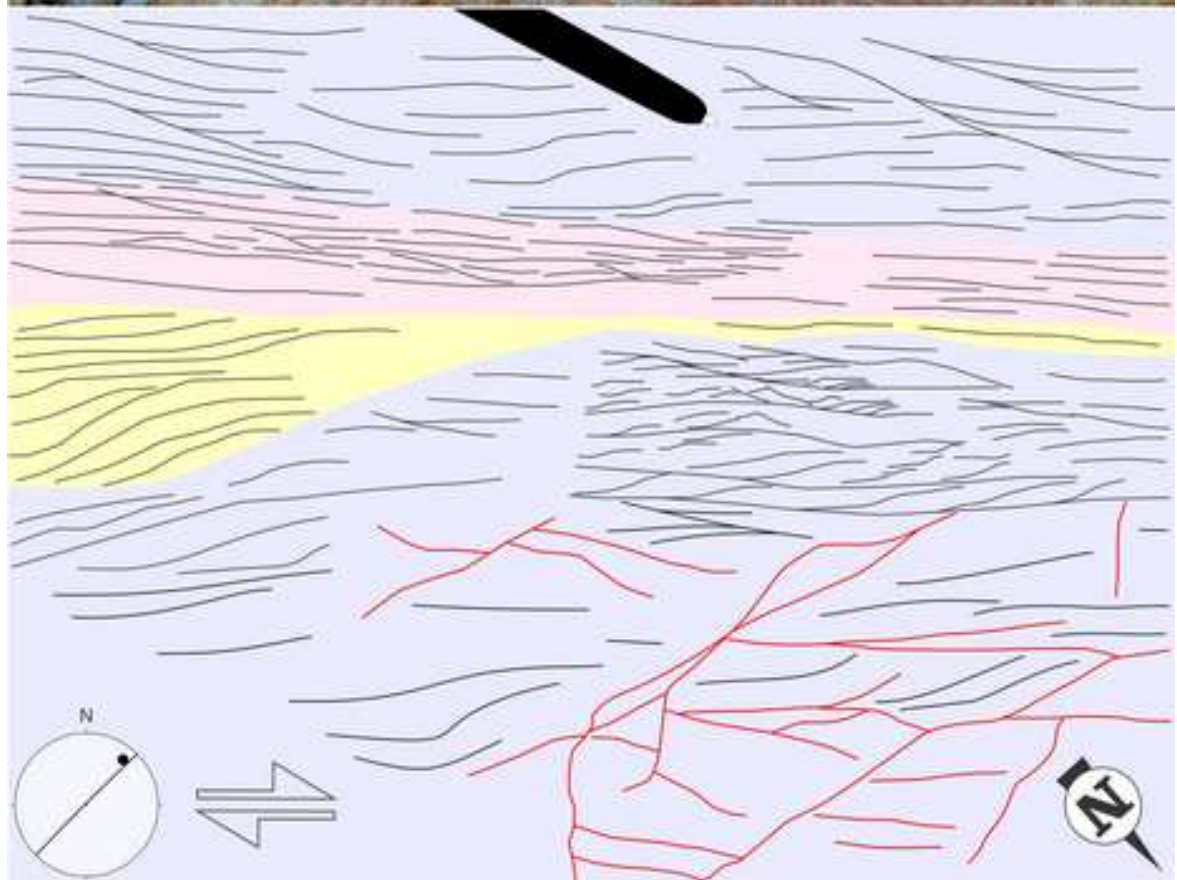


*Figure 5g

[Click here to download high resolution image](#)



Legend:
■ Granite gneiss ■ Aplite mylonite ■ Pegmatite gneiss - Main fault surfaces ▨ Mylonitic foliation

*Figure 6ab
[Click here to download high resolution image](#)

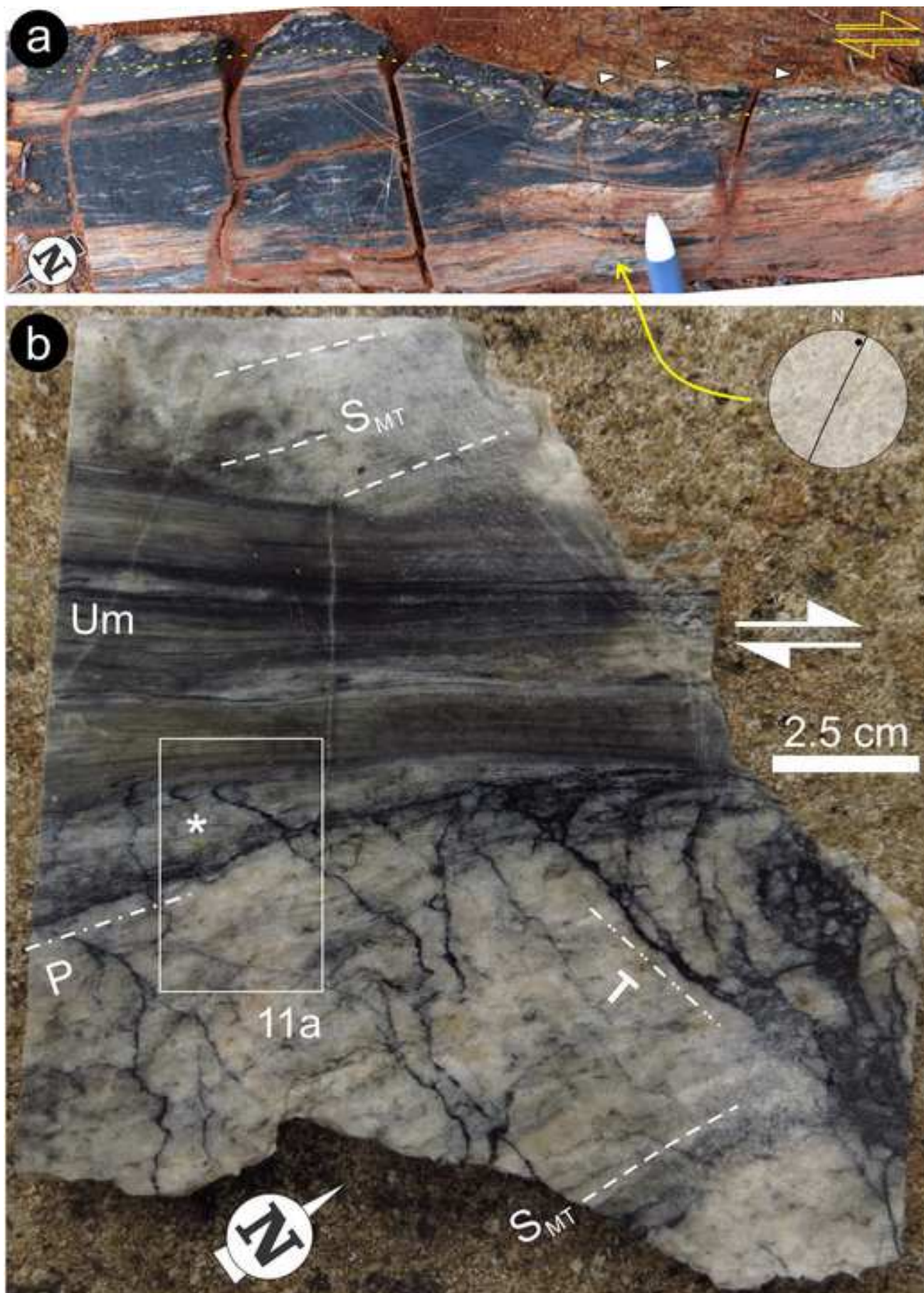


*Figure 7
[Click here to download high resolution image](#)

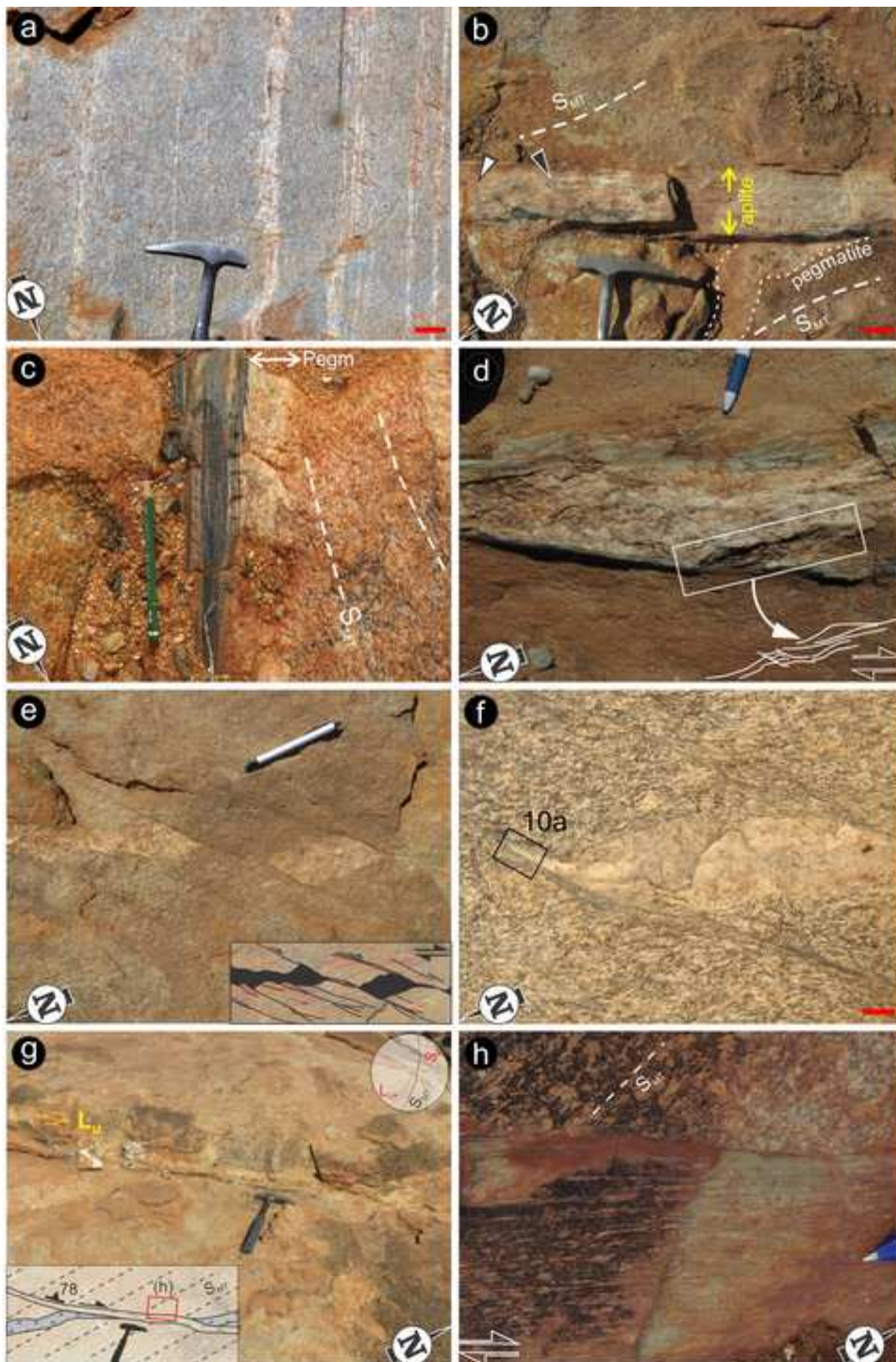


*Figure 8
[Click here to download high resolution image](#)

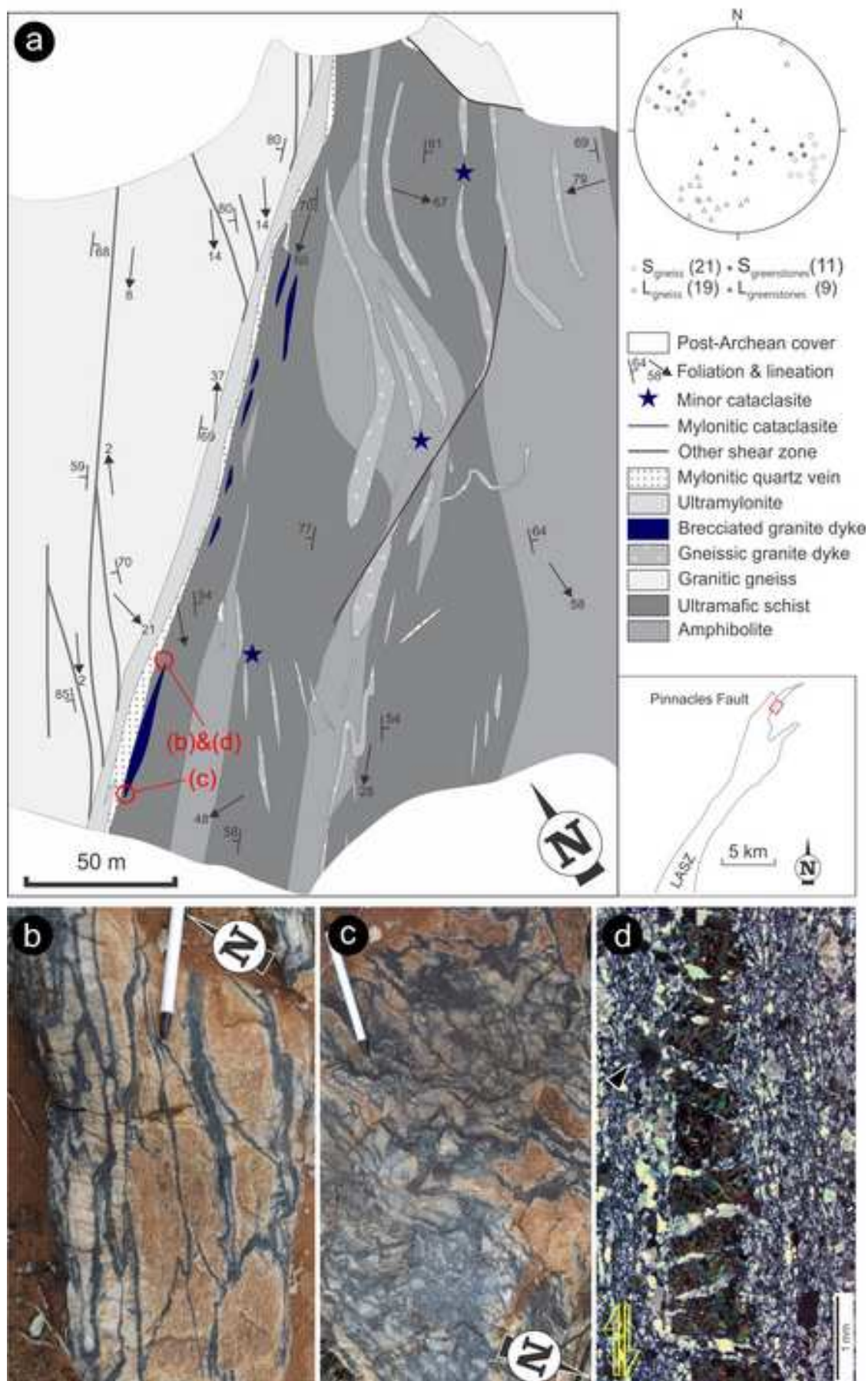


*Figure 9ac

[Click here to download high resolution image](#)

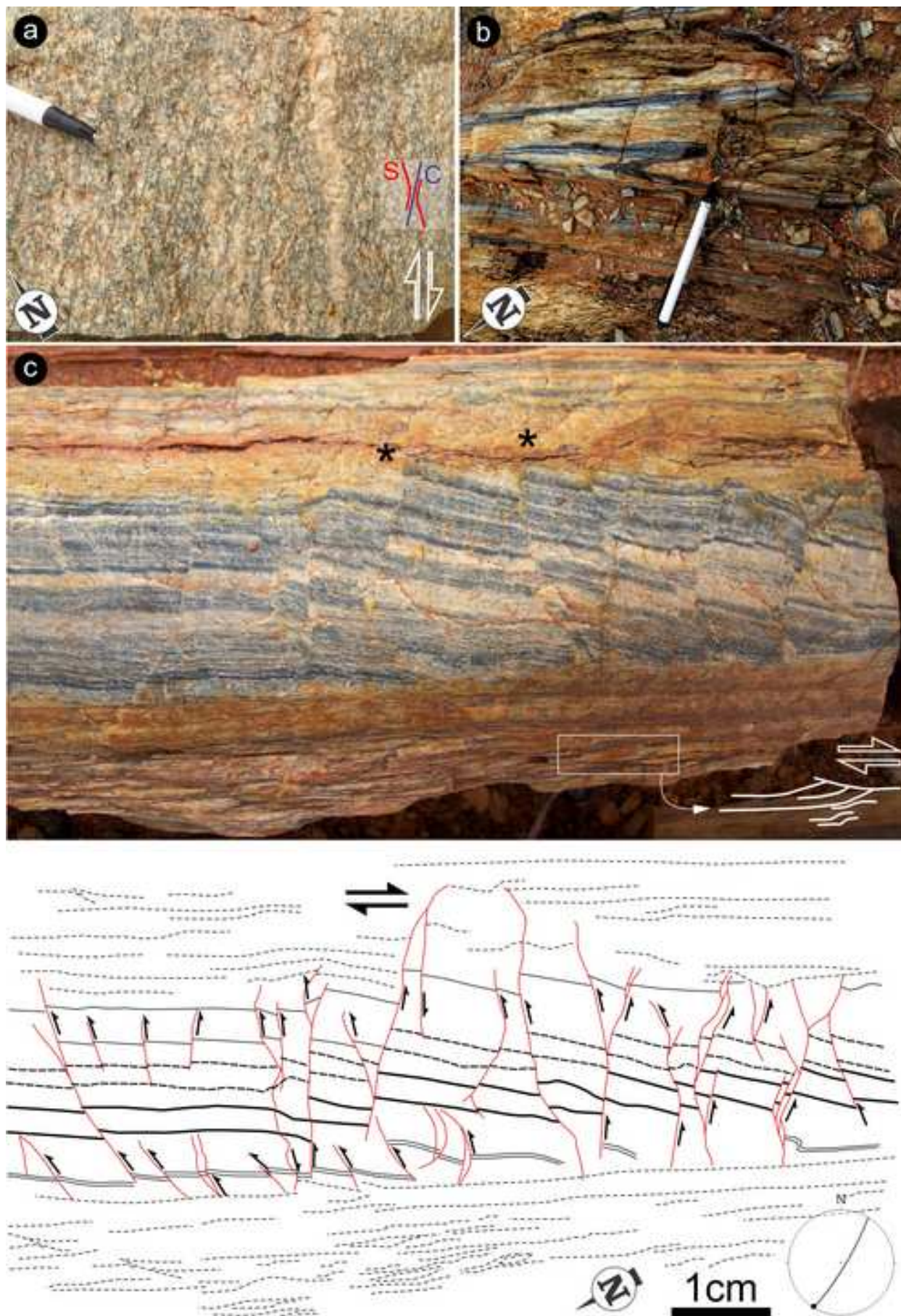


*Figure 9df
[Click here to download high resolution image](#)

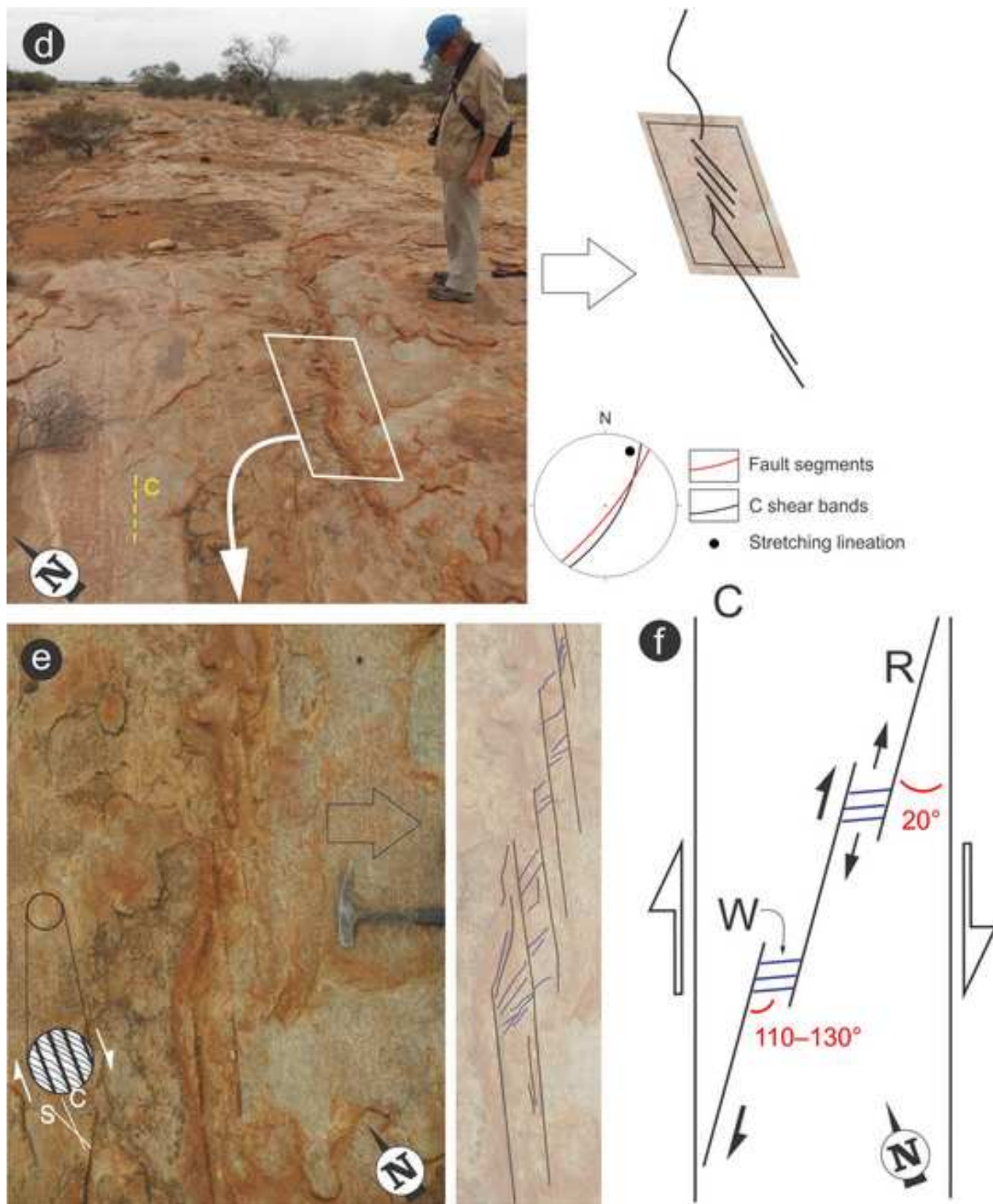


*Figure 10
[Click here to download high resolution image](#)

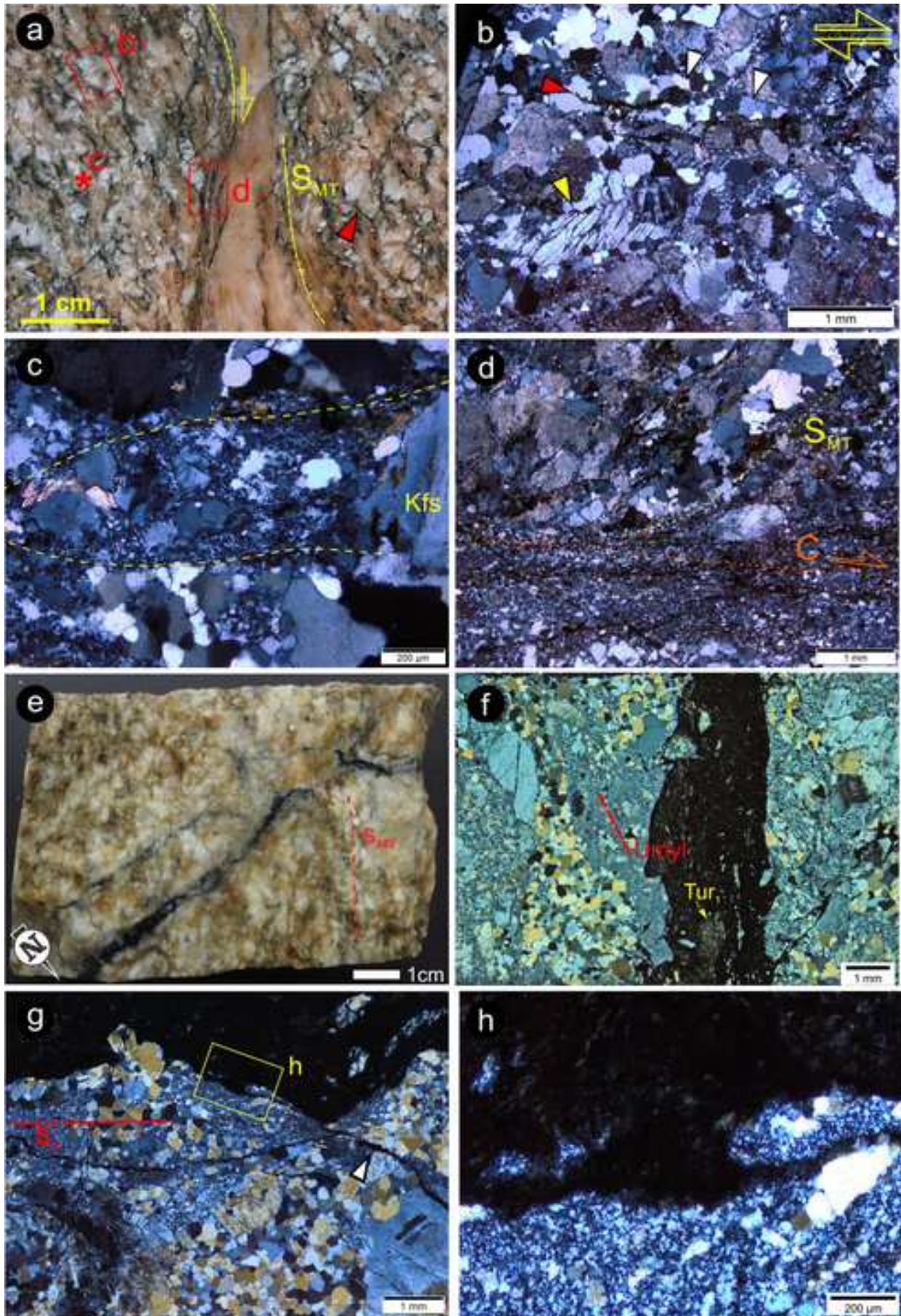


*Figure 11ae
[Click here to download high resolution image](#)

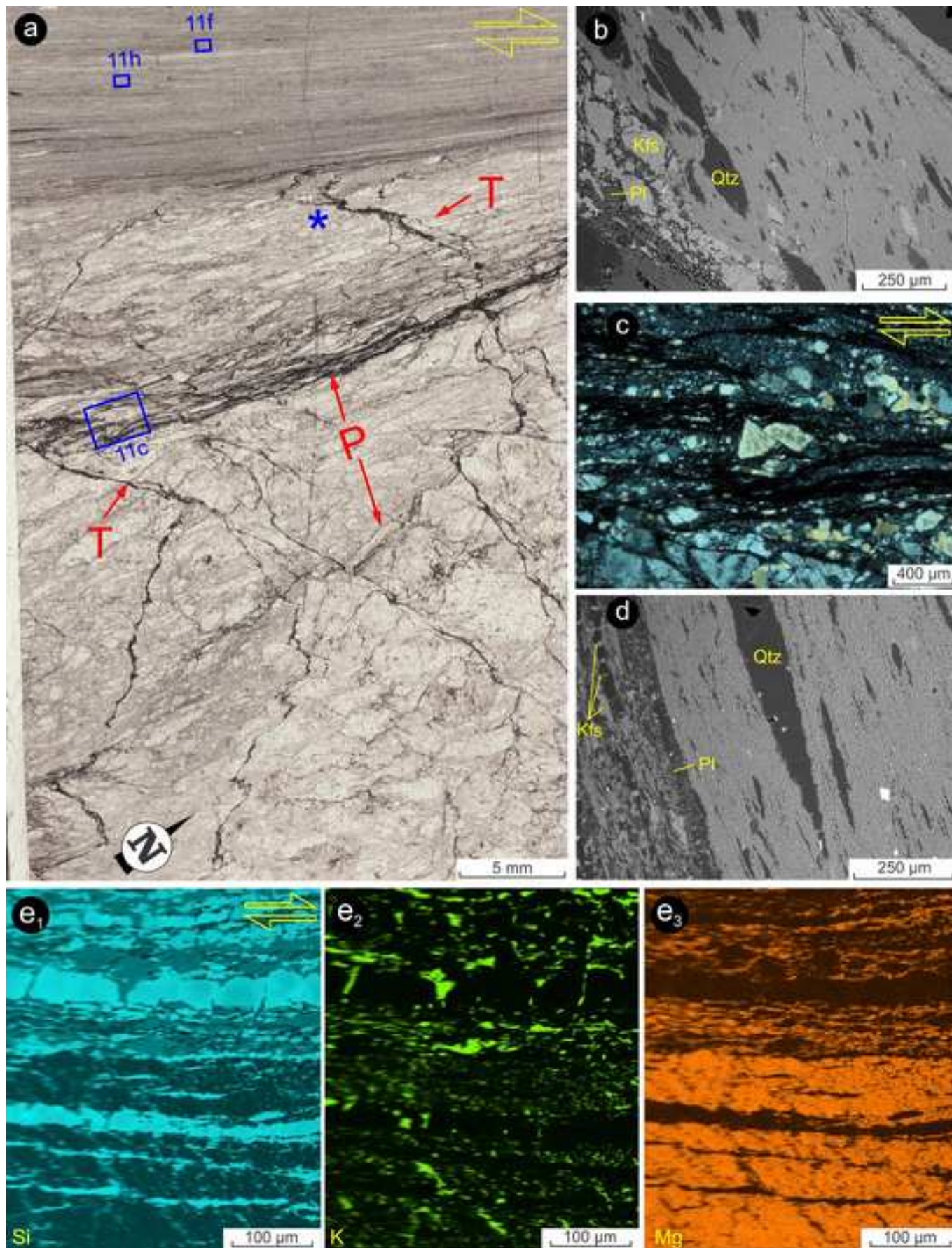


*Figure 11fi
[Click here to download high resolution image](#)

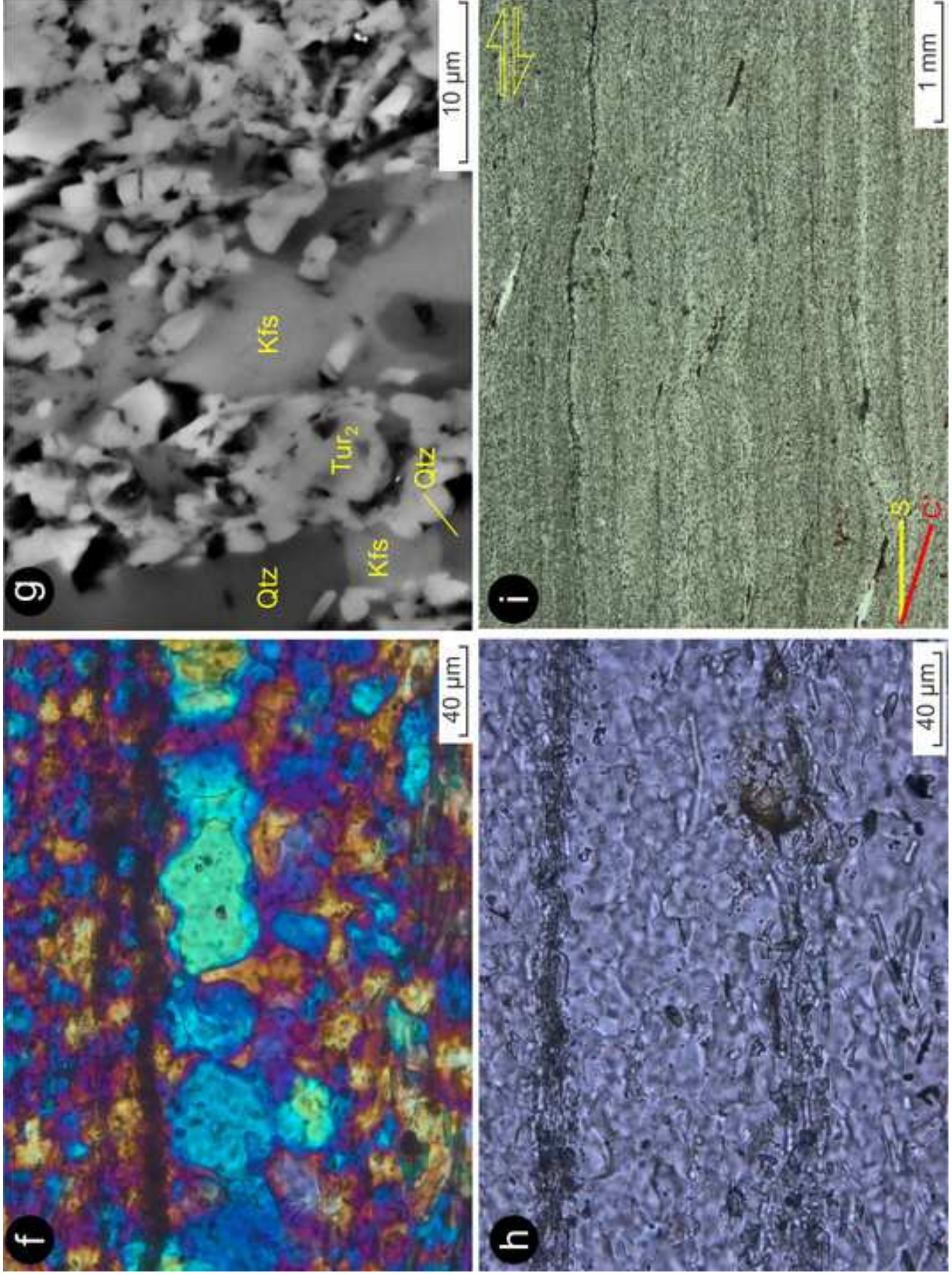


*Figure 12

[Click here to download high resolution image](#)

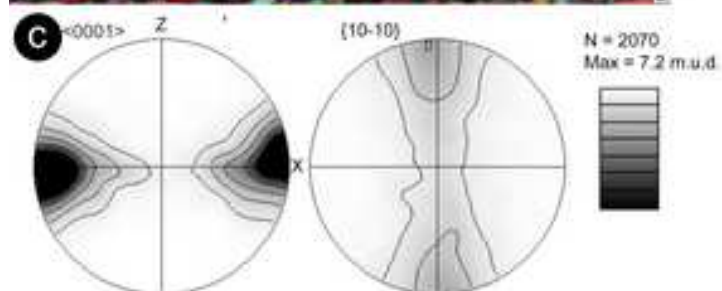
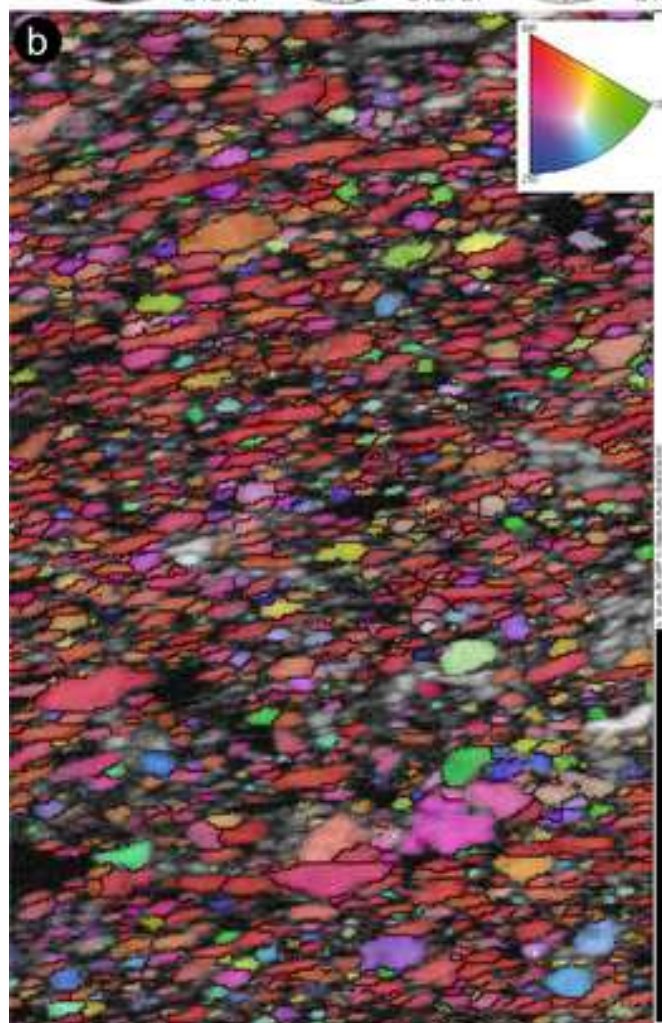
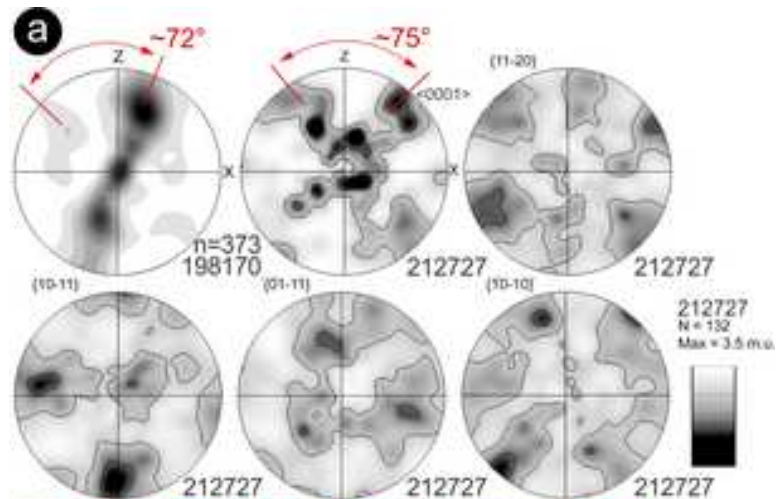


*Figure 13
[Click here to download high resolution image](#)

